University of Stavanger

Faculty of Science and Technology

MASTER'S THESIS

Study program/Specialization: Petroleum Geosciences Engineering	Spring semester 2019 Open
Author: Umedzhon Kakhkhorov	
Faculty supervisor: Wiktor Waldemar Weibull External supervisor: Pierre Yves Raya	
Title of thesis: Seismic imaging with primaries and multiples	
Credits (ECTS): 30	
Keywords: Depth imaging Velocity model building Multiple reflection Reverse time migration Full wavefield migration	Pages: 85 Stavanger, June 15, 2019

Seismic imaging with primaries and multiples

By

Umedzhon Kakhkhorov

MSc Thesis

Presented to the Faculty of Science and Technology

University of Stavanger

2019

Acknowledgements

Seismic imaging with primaries and multiples

Umedzhon Kakhkhorov

The University of Stavanger, 2019

Supervisor(s): Wiktor Waldemar Weibull, Pierre Yves Raya

Abstract

Multiples are usually considered as noise in seismic images due to their interferences with primary reflections. In recent years, new imaging methods have been developed which consider multiples as secondary sources to improve the subsurface image.

In the present study, we considered the advantages related to incorporating multiple reflections into imaging process, and presented a workflow for understanding the contribution coming from the different reflection events: primaries, surface-related and internal multiples. The workflow consist of two main parts: velocity model building, and imaging with Reverse Time Migration (RTM) and Full Wavefield Migration (FWM).

The workflow was tested on the synthetic and field datasets. Before actual imaging, the combination of first arrival traveltime tomography and full waveform inversion were used to obtain high-resolution velocity models. RTM imaging with primaries provides a good illuminated subsurface image with a broader frequency spectrum for the specific target interval. In the depth interval with the complex geological settings, primary images are distorted due to imperfect multiple separations. When imaging with surface-related multiples, the added value is observable at the shallow depths. However, the deeper part of surface-related multiple poorly illuminated comparing with the primary image. The added value coming from the internal multiples are clearly defined when implementing FWM on the synthetic data, in the depth interval with the notable velocity decrease FWM provides a more enhanced image. Application of FWM with 2D assumptions on the actual 3D data cannot provide a comparable image with RTM.

Table of Contents

List of Tables

List of Figures

1. Introduction

1.1. Background

It is well-known that reflection seismology plays a key role in exploration for hydrocarbons. Improvement in seismic processing and imaging methods have been made to enhance the images of the subsurface, leading to more accurate decisions through the Exploration and Production chain. With ongoing depletion of old fields and low risk prospects already discovered, the industry moves towards exploration in more complex geological settings. In the end, the geoscientists are pushed to use more advanced techniques to get better data, in order to improve their understanding of the subsurface.

Information extracted from seismic data, reflection events are mostly treated as primary- or multiple-based on whether the receiver-side wavefield experienced one or more reflections in the subsurface (Dragoset and Jeričević, 1998). Multiples are subdivided into surface-related and internal types. Historically, primaries have been considered as signal and multiples as a coherent noise. During processing, multiples are usually removed prior to migration, inversion or AVO analysis (i.e., before extracting subsurface information from primary reflections).

A significant challenge in getting better subsurface images is multiples (Weglein et al., 2011). Multiple reflections are usually considered as noise in the seismic images due to their interferences with primary reflections. There always will be some residual multiple energy in the seismic images, because there are no perfect multiple-removal methods. Over the years, the main goal of seismic interpretation was to understand subsurface geology by using the primary reflection events, and multiples were recognized as artifacts and interpretation pitfalls.

Both primaries and multiples contain information (Berkhout, 2014). Recent advances in processing technology have demonstrated the benefit of using multiples as valuable information to improve the image of the subsurface for petroleum exploration. Indeed, multiples reflection illuminate different parts of the subsurface compared to primaries leading to a richer scattering angle content in the pre-stack domain (Lu et al., 2015). Wave propagation is better represented when imaging with multiple waves and results in seismic images that more accurately characterize the subsurface

.This information becomes essential in more complex exploration areas that involves for instance, fault shadow area, salt diapirism or overthrust tectonics.

1.2. Thesis objectives

In recent years, efforts have been made to investigate the contribution of all multiple energy and compare different methods that use multiples for subsurface imaging. Nevertheless, one still needs to understand the benefits brought by imaging with multiples. The main objective of this study is to understand advantages and compare post-stack images with and without contribution from multiple reflections. This done using Reverse Time Migration (RTM) and Full Wavefield Migration (FWM). The specific objectives of this study are:

- Develop a robust velocity model building workflow based on FWI. FWI provides an accurate and detailed velocity model which potentially allows the creation of high-quality subsurface images in depth;
- Propose and practically test imaging workflows with surface-related multiples using RTM method to enhance the shallow image of the subsurface;
- Compare and define the value of imaging with different reflection events: primary itself, surface-related multiples and total data (i.e. primary, surface-related and internal multiples).

1.3. Seismic events classification

In this section we briefly describe the different seismic events which are observed in a shot record (seismogram), due to a wavefield initiated by a single source and measured by many receivers and discuss the contributions of these events when imaging the subsurface.

Seismic wavefield is recorded as a seismogram by many receivers, which are located on the Earth's surface or towed at a certain depth below sea level for land and marine seismic configurations, respectively.

Seismograms consist in groups of traces showing certain seismic waves (i.e. coherent events recognized by a systematic amplitude or phase change). Figure 1.1 shows examples of a field record acquired at the Barents Sea (Figure 1.1a). We can observe that each seismic event can be recognized by its traveltime and amplitude characteristics. Typically, there are three main types of waves which can be distinctly seen on the seismic marine record (Figure 1.1b): direct wave, refracted (or guided) waves and reflected waves. There are more number of seismic waves depending on the subsurface conditions and acquisition parameters. Liner (2016) discussed some general classification for seismic events.
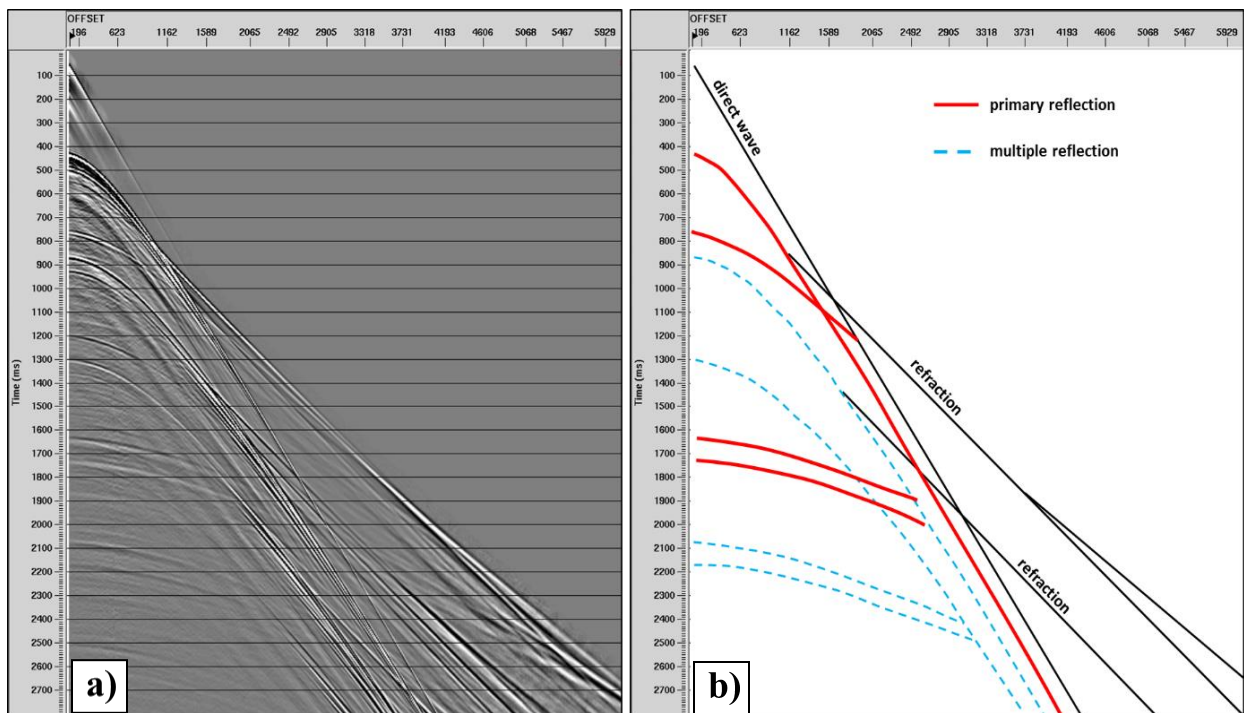
Figure 1.1: *A common shot gathers (a) and its sketch showing main seismic events (b).*

The events that contribute to the image created by standard migration algorithms are shown in the black bold font (Figure 1.2). Those are - diffractions and primary reflections (signal). All other events are considered as "noise" and removed prior to the imaging process. The main goal in conventional processing is to enhance a signal by attenuating all other events, which are coherent and random noises. This is done by using specialized signal processing algorithms (Yilmaz, 2001).
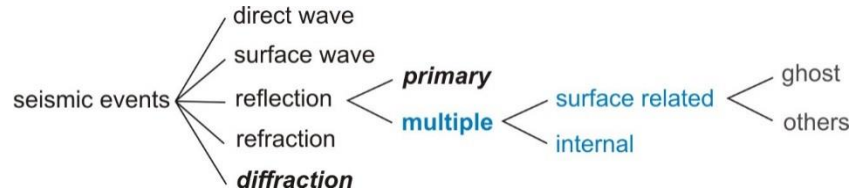
Figure 1.2: *A classification tree for seismic events (Liner, 2016).*

According to the Huygens' principle, when a wavefront arrives at a certain point, that point will behave also as a source for the new wave, and so will all its neighbors (Liner, 2016). The new wavefront is then the superposition of all the waves which were generated by these points (scatterpoints). In a marine seismic survey, the primary reflection, emitted from air-gun array, bounces from a reflection point (sea bed, geological layers), and travels back to the water-air interface (upgoing wavefield). We can interpret this surface (water-air interface) as a set of secondary sources that emits the upgoing wavefield back into the subsurface (downward wavefield) such that primary reflection events become first-order multiples, first-order multiples become second-order multiples, etc. Every multiple reflection can be considered as a natural-blended response of the subsurface and consists of superposition of a primary reflection with another primary or a multiple reflection (Berkhout and Verschuur, 2006).

Classifications of multiples is mostly accomplished by using differences in the properties of multiple reflections to discriminate between them. One distinction is between surface-related and internal multiples (Dragoset and Jeričević, 1998). If the multiple bounces at least one time at water-air interface (i.e. the free surface), it is called a surface-related multiple (Figure 1.3, blue lines). This type of multiple can be categorized by the number of times it has undergone reflection at the free surface as first order (Figure 1.4, dashed red line), second order (Figure 1.4, dashed magenta line), and so forth. Internal multiples, on the other hand, have all of their downward reflections bounced at the water bottom or below the reflector inside the subsurface (Figure 1.3, green line). This type of multiple gets more attention for the deep reservoirs like when the exploration target is a subsalt or a sub–basalt layer (Liu et al., 2011).
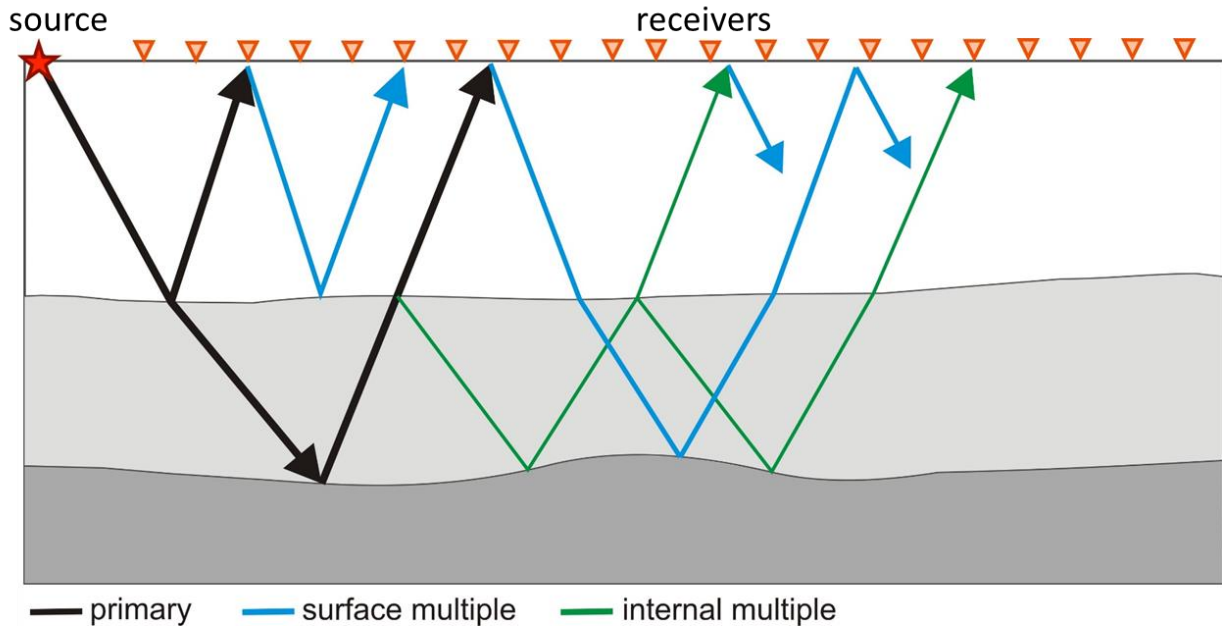
Figure 1.4: *Schematic description of primary and multiples reflections.*
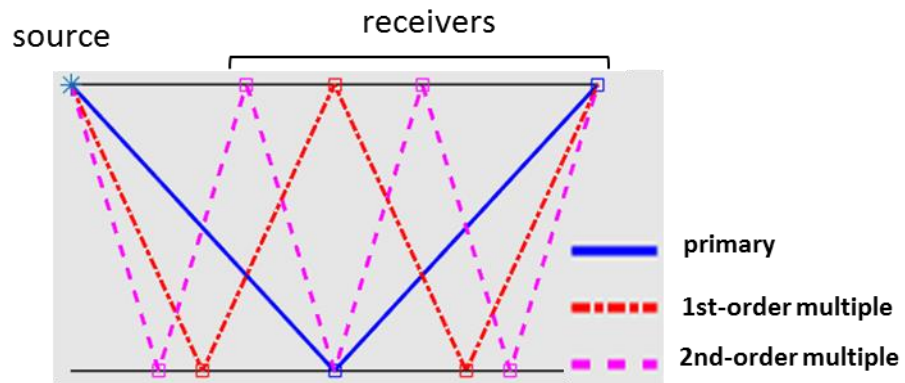
Figure 1.3: *Schematic description of multiple orders.*

Due to a more complex wave path, multiples cannot be imaged by conventional methods designed for primary reflections and therefore often treated as noise. The geophysicists are very well familiar with some types of multiples, for example, receiver- and source-side ghosts and water-layer reverberation. In this work, only the imaging of surface-related and internal multiples are considered.

1.4. Imaging with multiples

The reflection seismic methods involve three main processes - data acquisition, processing and interpretation. Migration is the process of building the subsurface image from seismic data by proper focusing and spatial positioning the observed seismic data into its true (ideally) geological position (Yilmaz, 2001), .i.e. using recorded seismic data to reconstruct the reflectivity (i.e. impedance contrast) distribution. Then this distribution is used to understand the subsurface geology. Migration is performed either in time or depth domains using pre-stack and post-stack seismic data (Yilmaz, 2001). The difference between time and depth migration is that depth migration takes into account lateral velocity changes while time migration ignores these. In order to produce high quality image with true geological depth, it is very important for depth migration to use an accurate velocity model which honors correctly the subsurface geology (Jones, 2010).

The significant difference of depth migration is that the velocity estimation becomes an integral component of the migration process and usually depth migration is referred as seismic imaging. Imaging is the most important and complex step in seismic processing. It is also the most data-intensive component with the highest computational requirements. Imaging is the result of two processing steps that are tightly connected: wavefield reconstruction (i.e. migration) and imaging condition. Compared with migration, the seismic imaging process is usually referred as an iterative process of velocity model building combined with migration (Jones, 2010).

Currently there are two views regarding multiple reflections: (1) the conventional view and (2) the innovative view. The conventional view considers primary reflections as signal and multiples as coherent linear noise (Dragoset, 1999; Wiggins, 1988). The main reason why multiples are classified into noise category is their complex path through the subsurface. When multiples are not taken properly into account, they can distort the image leading to inaccurate interpretation. In that view, the capability of attenuating all multiple reflection energy from seismic data mostly defines the quality of the subsurface image (Weglein et al., 2011).

The innovative view proposes that instead of considering multiples as noise they should be treated as a signal, modifying the imaging technique in such a way as to accommodate multiple reflections (Berkhout and Verschuur, 2006). In that view multiples are considered as secondary seismic sources to get improved subsurface illumination. Using demultiple methods do not guarantee perfect elimination of multiples. Indeed, the primary dataset will always contain some multiple residuals, meaning that presence of these residuals will distort the image because they have not properly been taken into account (Davydenko and Verschuur, 2017). This thesis is based on the innovative view approach, i.e. multiple reflections should be incorporated into seismic imaging.

Each multiple reflection is related to the primary event from which it originated. Most multiples can be distinguished from primaries due different properties: periodicity, difference in moveout, weak amplitudes (Dragoset et al., 2010). From Figure 1.5a we can notice that multiples are perfectly periodic at zero offset, but with increasing offset, they are not periodic. This property of multiples are usually used in predictive deconvolution to attenuate repeating multiples at near offset (Yilmaz, 2001). In a simple horizontal model when velocity increases with depth multiples have almost the same normal-moveout velocity but arrive at later times than the primaries (Figure 1.5a, multiples have same trajectory). However, in complex geological setting (i.e. when the velocity can decrease with depth) multiples are often superimposed with primaries and using velocity to distinguish multiples from primaries is very challenging. It is one of the main reasons why demultiple algorithm based on different moveout behavior are less effective in complex geological environment (Ikelle and Amundsen, 2005).
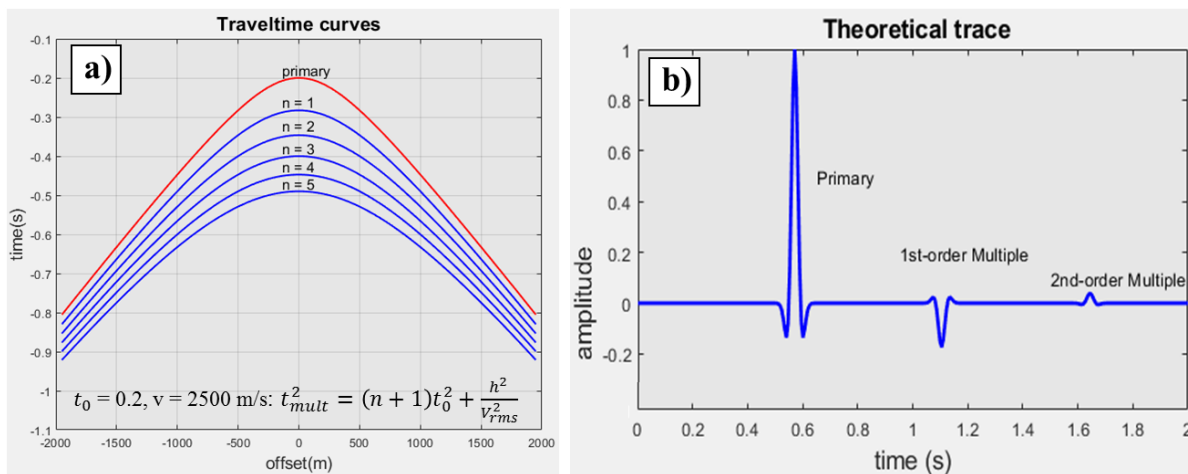
Figure 1.5: (a) The traveltime curves for the primary and first five multiples, (b) Theoretical trace showing relation between primary and surface related multiples for two-layer model.

7

Generally, the amplitude of the multiple waves is weak comparing with primaries due to amplitude decay with distance, scattering (transmissions losses and mode conversion). Figure 1.5b show the theoretical trace modeled for a point source. We can clearly see that primary event has larger amplitude. The amplitude of multiple event is roughly proportional to the reflectivity of the reflector from which it generated and in most cases always lower than the amplitude of primary event. In the medium with strong velocity contrast (i.e. presence of salt bodies, unconformity surfaces) it is possible to observe the stronger multiple reflections than primaries (Yilmaz, 2001).

For a given single shot experiment, multiples can lead to an increase in subsurface illumination and better angle coverage. Figure 1.6 shows that a subsurface point is illuminated several times when using primaries and multiples (i.e. higher fold). This results in a better quality of the seismic image, i.e. wider subsurface illumination and increase in the reflectors continuity (Schuster, 2009). For a given source-receiver pair, primaries and multiples will have different reflection angles. Figure 1.6 demonstrates that primaries have a wider angle range while multiples propagate with more vertical angles. Imaging with multiples can enhance the angle-coverage of the image (Schuster, 2009). Having more vertical reflections can improve the illumination of shallow reflectors. However, a wide range of reflection angles is more important for imaging of the steep dip reflectors (Yilmaz, 2001). It means that using only multiples to fully illuminate complex structures is not enough and primaries are essential to image such structures.
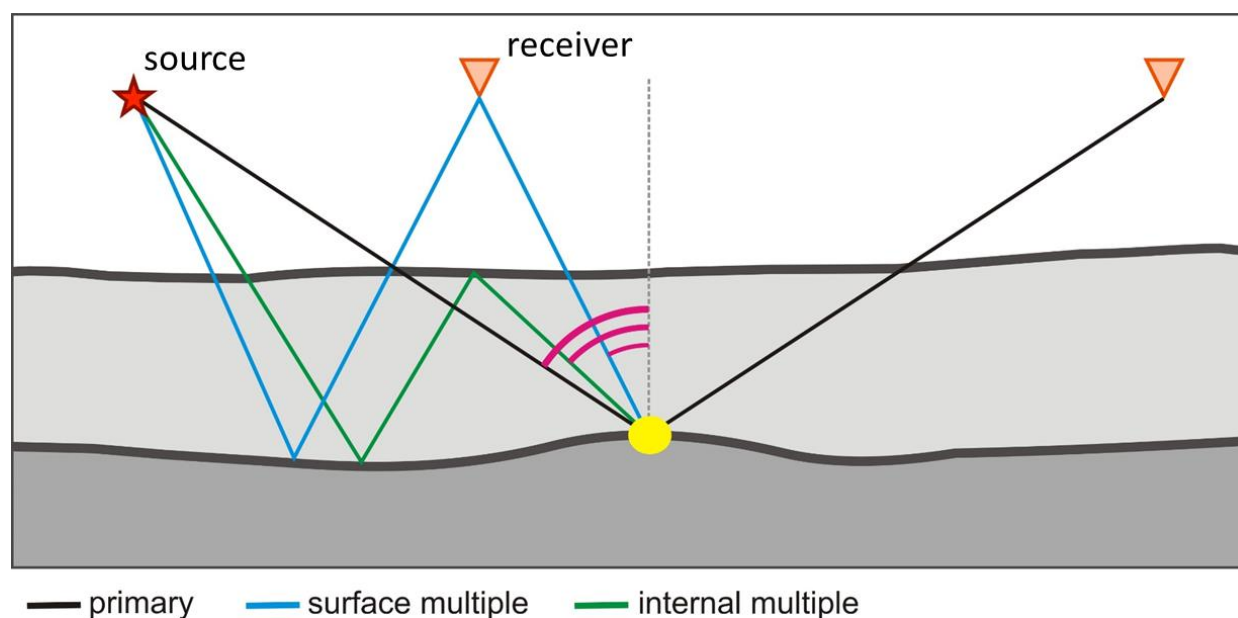
Figure 1.6: *Schematic diagram showing the illumination subsurface by using multiples.*

Imaging methods and algorithms with multiples differs from each other (including multiples directly or separate imaging of primaries and multiples). They also differ in the use of specific multiples (surface-related, internal or both). In recent years, many papers about imaging with multiples have been published (Berkhout, 2014; Malcolm et al., 2009; Whitmore et al., 2010).

In marine seismic, where we know the free surface location and its reflectivity value, incorporating surface multiples into the imaging process is relatively easy. In recent years, efforts have been made to perform imaging with surface-related multiples. The implementation of surface-related multiples with wave-equation migration has been shown by Berkhout and Verschuur (1994) and Guitton (2002). They show that the imaging principle of Claerbout can be extended to migrate the surface-related multiples. In this case, separated surface-related multiples are back propagated and cross-correlated with forward propagated primaries. This approach was adapted in imaging with separated wavefields (SWIM) (Lu et al., 2015) and in reverse-time migration of first-order surface multiples (Yang et al., 2015). Methods of interferometric imaging incorporating surface-related multiples for vertical seismic profile (VSP) data are well explained by (Schuster, 2009).

In the past decade, several migration algorithms have been developed to use internal multiples in imaging. (Malcolm et al., 2009) proposed a multi-pass approach based on one-way wave equation. Lu et al. (2015) developed a modified reverse-time migration where the imaging condition is applied to the decomposed source side and receiver side wavefield.

Berkhout (2014) proposed full-wavefield migration (FWM) which accommodates all orders of surface multiples as well as internal multiples. FWM makes use of two-way wave theory that is defined in terms of one-way wavefields (Davydenko and Verschuur, 2017). The algorithm aims at minimizing the difference between the modelled and the observed data by yielding subsurface reflectivity at every grid point of the subsurface.

In the present study, our methodology consists of reverse-time migration to investigate imaging with surface-related multiples. In order to understand the advantages of including higher order multiples as well as internal multiples, we compare this methodology with FWM

2. Theory

Advanced techniques are utilized in imaging of seismic data. It is important to understand (from a physical viewpoint) the theory behind these techniques when choosing the appropriate strategy and parameters for the imaging algorithm and the input data. Some concepts of the seismic method need to be reviewed, prior to approaching the full study. It includes coupling between primary and multiple waves, velocity analysis, seismic imaging algorithms and, imaging conditions.

2.1. First arrival tomography

First-arrival traveltime tomography (FATT) is an inversion algorithm that uses fist arrival traveltimes of direct or refracted waves to assess a velocity model (Zhu et al., 2008). The tomography method proceeds by calculating traveltimes through the velocity model and then updates the velocities by minimizing the difference between the modelled and observed traveltimes. Depending on the source-receiver distance (i.e. offset) deeper velocities could be assessed (Figure 2.1). Usually the first arrival tomography is used to estimate the velocity model up to 1 - 2 km kilometers (for 6 km offset data). In this work, we used tomography based on the adjoint-state method (Taillandier et al., 2009).
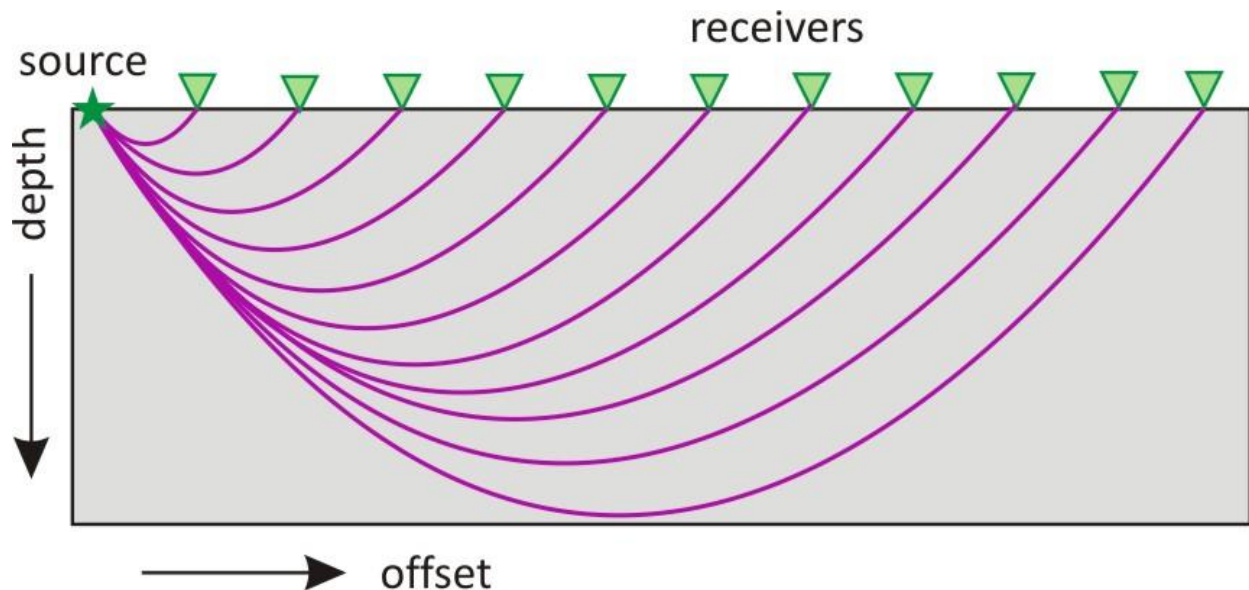
Figure 2.1: *Ray fan for a single shot. Rays traced in horizontally layered medium with constant velocity increase.*

The tomography is considered as a nonlinear optimization problem. The process aims at reducing the misfit function or the difference between observed T_{obs} and modelled t traveltimes (i.e. the solution of the Eikonal equation). The extended misfit function in case of adjoint method becomes (Taillandier et al., 2009):

$$L(v,t,\lambda) = \frac{1}{2}\int dr|t(r) - T_{obs}(r)|^2 - \frac{1}{2}\int dx\lambda(x)\left(|\nabla t(x)|^2 - \frac{1}{v(x)^2}\right),\qquad 2.1$$

where v is a velocity model, r is a receiver, variable λ is a term to ensure that at the optimum. We used a quasi-Newton gradient-based approach for minimization of the misfit function. Having the gradient of the misfit function ∇L, tomography can be formulated as a nonlinear problem:

$$v_{n+1} = v_n + a_n\nabla L(v_n),\qquad 2.2$$

where c_{n+1} is the optimal velocity, c_n is a given velocity model and a is a negative scalar.

Difficulties with refraction tomography are related to the quality of first arrivals. Depending on the geological setting, first arrivals could be challenging to pick. Another important issue is the initial velocity model. If the initial model is too far from true model, the inversion could lead to an unrealistic model (Taillandier et al., 2009).

2.2. Full Waveform Inversion

Full waveform inversion is a non-linear optimization procedure (i.e. data-fitting) that seeks to find the velocity model by minimizing the difference between recorded and modelled seismic waveforms (Figure 2.2). Lailly (1983) and Tarantola (1984) developed seismic inversion algorithms as an optimization problem. They show that based on the gradient methods an updated velocity model can be obtained by minimizing an objective function based on the difference between modelled and observed seismic waveforms. In recent years, several examples of successful application of waveform inversion in real seismic datasets have been shown (Sirgue et al., 2009; Virieux and Operto, 2009).
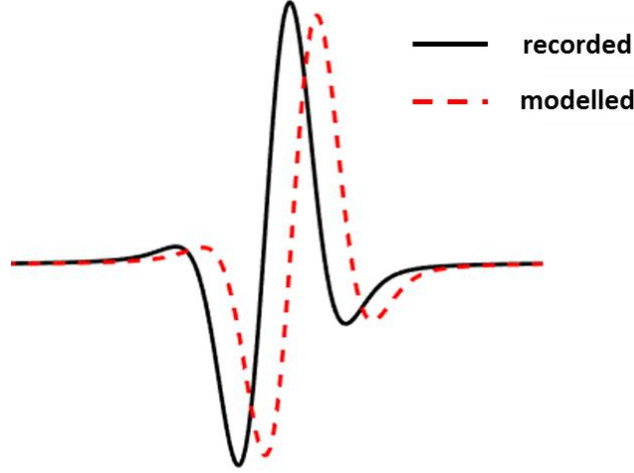
Figure 2.2: Recorded and modelled seismic waveforms.

The synthetic data in FWI is modeled through the numerical solution of a wave equation. FWI can be implemented using any wave equation, such as the acoustic, visco-acoustic and elastic wave equations (Virieux and Operto, 2009). In this study, inversion is carried out using the acoustic approximation of the wave equation:

$$\frac{1}{V^2}\frac{1}{\rho}\frac{\partial^2 P}{\partial t^2} = \left[\frac{\partial}{\partial x}\left(\frac{1}{\rho}\frac{\partial P}{\partial x}\right) + \frac{\partial}{\partial y}\left(\frac{1}{\rho}\frac{\partial P}{\partial y}\right) + \frac{\partial}{\partial z}\left(\frac{1}{\rho}\frac{\partial P}{\partial z}\right)\right] + S,\qquad 2.3$$

where $P(x, y, z, t)$ is the seismic data, $\rho(x, y, z,)$ is the density, S is the source at locations $(x, y, z,)$ and V is the velocity model. The time is denoted by t. A finite-difference method is used for the numerical solution of equation. 2.3. Given a velocity model and source locations, the solution of the acoustic wave equation is the modeled seismic data restricted to compressional or P-waves (no shear waves).

The least-squares sum of the difference between the recorded and modelled seismic data is the misfit function (i.e. the objective function). In the waveform inversion scheme the objective function is optimized, aiming to minimize the misfit between recorded and modelled data (Virieux and Operto, 2009). In this study, we used a global-correlation-based objective function (Choi and Alkhalifah, 2012):

$$S = \sum_{i}^{sn}\sum_{j}^{rn}\left[-\widehat{P}_{i,j} \cdot \widehat{P}_{i,j}^{obs}\right],\qquad 2.4$$

where rn and sn are the number of receivers and shots, $\widehat{P}_{i,j} = P_{i,j}/\|P_{i,j}\|$ is the modelled data for the ith shot and jth receiver, $\widehat{P}_{i,j}^{obs} = P_{i,j}^{obs}/\|P_{i,j}^{obs}\|$ is the observed data. The notation '$\| \quad \|$' indicates the normalization of the wavefields. The gradient of the misfit function S provides the direction of minimization along which the velocity disturbances is searched, i.e. provides the direction to move from the initial model to an updated model. The velocity model is then iteratively updated using the gradient of the misfit function $G = \nabla S$ with a step-length λ_n and can be mathematically expressed by:

$$v_{n+1} = v_n - \lambda_n G_n, \qquad\qquad 2.5$$

where v_{n+1} is the updated model, v_n is an initial model, and λ_n is a positive scalar.

The main limitation of waveform inversion is that it suffers from cycle skipping problems, i.e. the convergence towards local minima instead of the global minimum because of an inaccurate starting model, the absence of low frequencies and the presence of noise (Virieux and Operto, 2009). Common approaches to avoid cycle skipping problems are to use an initial velocity model estimated using refraction tomography, and implementing a multi-scale strategy to progressively input frequencies and/or offsets (Sirgue and Pratt, 2004).

A full mathematical development of the FWI theory can be found in the literature by Tarantola (1987) and Fichtner (2011).

2.3. SRME

As we mentioned before, one of the main objectives of this study is to incorporate surface-related multiples into seismic imaging. In this section, we discuss the separation of surface-related multiples from the total reflection response. For removing multiples, we used the surface-related multiple elimination method (SRME) which is a data-driven technique for predicting and subtracting all surface-related multiples (Verschuur, 1991).

SRME is a method for attenuating the multiples generated by the free surface, i.e. when secondary downward reflection occurs at the water-air contact. It uses the observed data to predict all surface-related multiples. Then, in a separate flow the predicted multiples are subtracted from recorded data using adaptive filtering.

13

The main advantage of SRME over other demultiple algorithms (radon, deconvolution, wave equation prediction) is that SRME makes no assumptions about multiple reflection properties, i.e. moveout and periodicity (Verschuur, 1991). Most of the demultiple techniques require also some knowledge (velocity model) about the subsurface prior to removing multiples, while SRME does not. The implementation of SRME assumes that the free surface is a perfect reflecting boundary with reflection coefficient -1, and that the input data is regularized prior to modeling the multiples.

SRME is based on auto-convolution of observed data with itself to predict the surface-related multiples from the data. In this method, surface-related multiples which always have a reflection point at the free surface are subdivided into two primary events (Figure 2.3a). We can then predict a surface-related multiple by convolving these two primaries. Each different type of surface-related multiple need two different primaries to combine in order to predict the multiples (Figure 2.3b). For a given source gather (Figure 2.3b, orange lines) and receiver gather (Figure 2.3b, blue lines) SRME considers all possible reflection points at the free surface, convolves all possible combinations, and then the summation will produce all surface-related multiples for the given source-receiver pair. This procedure is repeated over all shots and receivers. The 2D process of predicting the multiples is given by (Dragoset et al., 2010):

$$M(x_s, x_r, t) = r_o \sum_{x_k} r(x_k, x_r, t) * d(x_k, x_s, t), \qquad 2.6$$

where $*$ means convolution in time, r_o is the reflection coefficient, $r(x_k, x_r, t)$ and $d(x_k, x_r, t)$ describe receiver and shot gathers, respectively. The predicted multiples are denoted by $M(x_s, x_r, t)$, the spatial coordinates by x.

Ideally, the output of SRME should contain all surface-related multiples (i.e. first-order, second-order, etc.), but due to imperfect adaptive subtraction, either residual primary signal could be presented in the multiple model or not all surface-related multiples are eliminated (Dragoset et al., 2010).
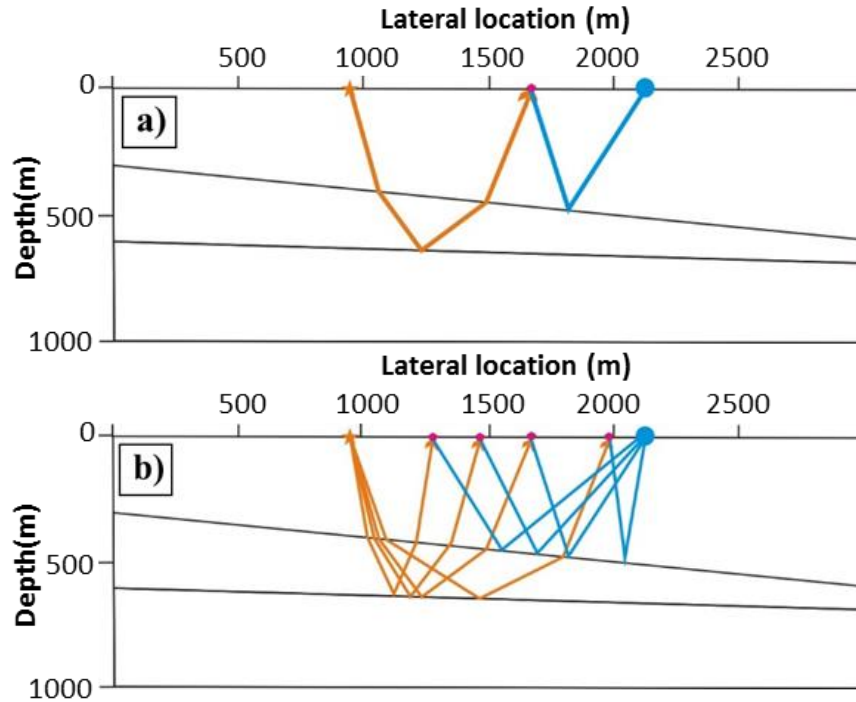
Figure 2.3: (a) Convolution of two primaries resulting in a surface-related multiple and (b) multiples can be predicted by summing convolution results of shot (red lines) and receiver (blue lines) gathers (modified from Dragoset et al. (2010)).

2.4.   Least-squares reverse time migration

Reverse time migration (RTM) was originally proposed by several authors (Baysal et al., 1983; Whitmore, 1983), and until after 2000s its implementation was limited due to a high computational cost. In this study, we used RTM based on a two-way solution of the acoustic wave equation. RTM can correctly account for the wave propagation effect and produce an accurate and high-resolution subsurface images in complex geological settings. Currently, application of RTM have become a widely accepted technique for primary imaging, the algorithm can handle wide-angle reflections and produce much cleaner images comparing with other migration methods (Leveille et al., 2011).

According to Claerbout's principle (Claerbout, 1985), the reflector position is defined by cross-correlating the source (downgoing) wavefield with the receiver (upgoing) wavefield (figure 2.4). In RTM method, migration involves reconstruction (i.e. extrapolation) of a source wavefield down

from source location into the earth and the reconstruction of the recorded receiver wavefield back from receiver location into earth (figure 2.4).
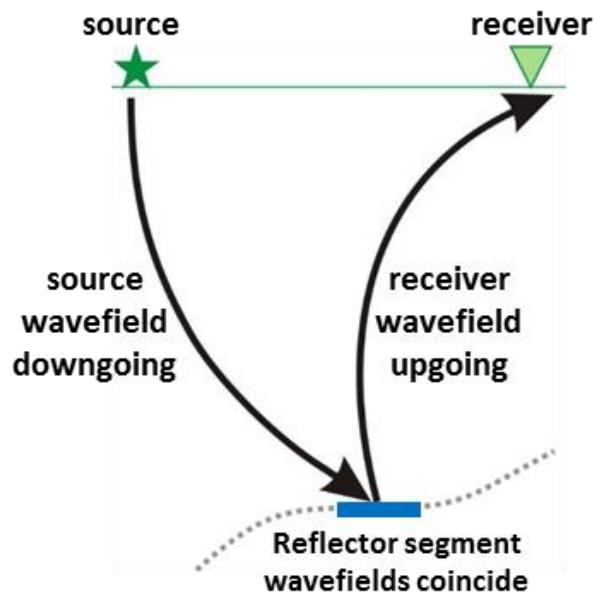
Figure 2.4: Schematic diagram showing imaging condition.

The main difference of RTM compared to wave-equation migration is that both source and receiver wavefields extrapolated in time, not just in the vertical direction. This permits waves to travel in all direction and illuminate better steep and complex geological structures (faulting, salt tectonics).

The RTM consists in three main steps:

- Computing source side wavefield $P_D(x_r, t; s)$ over all shots s and receiver coordinates x_r. Knowing velocity model and source signature, the downgoing wavefield is modelled using acoustic wave equation.
- Computing receiver side wavefield $P_U(x_r, t; s)$. Recorded seismic data $P^{obs}(x_r, t_{max}; s)$ is backward extrapolated from t_{max} to $t = 0$.
- Computing image by applying an imaging condition: reflector position defined when source side and receiver side wavefield coincide (i.e. interfere) in each step of time and space.

More recently, RTM has been used to incorporate multiples, especially first-order surface-related multiples (Yang et al., 2015). To image surface-related multiples, standard RTM implementation

16

is modified and primary dataset (i.e. multiple free) as source side wavefield and first-order surface-related multiple (i.e. eliminated multiples from observed data) as receiver side wavefield. A summary of RTM application for primary and surface-related multiples is given in Table 2.1.

Table 2.1: *RTM methodology for migrating primaries and first-order surface multiples.*

reflection event	wavefield		imaging condition
	source side	receiver side	
primary	point source to model wavefield	recorded data back propagated	cross-correlation imaging principle
first-order surface-related multiples	primary dataset as a surface source	subtracted multiples recorded data	

RTM images are usually contaminated with artifacts due to the propagation operator. For example, low-frequency artifacts are generated when the velocity field has strong contrasts (Leveille et al., 2011). The common approach to avoid these artefacts is to apply RTM as a least-squares inversion instead of a migration. Least-squares migration was first proposed by (Nemeth et al., 1999) where they considered migration as a linear problem, the aim being to match the recorded data and improve focusing and amplitude accuracy.

In this study, we used the least-squares RTM (LSRTM) approach proposed by (Weibull and Arntsen, 2014). LSRTM aims to iteratively update the subsurface image by:

$$I_{n+1} = I_n - \alpha_n \frac{\partial S}{\partial I}, \qquad 2.7$$

where I is an image, n is number of iteration and α is a step length. The gradient is denoted by $\frac{\partial S}{\partial I}$. After each iteration the image becomes sharper, has better amplitude distribution and the low-frequency artifacts are removed. The gradient produced by cross-correlation of source side P_D and residual P_λ wavefields:

$$\frac{\partial S}{\partial I} = \sum_t P_D(x_r, t; s) * P_\lambda(x_r, t; s), \qquad 2.8$$

where P_D modelled using acoustic wave equation given a source signature $S(x, t)$:

$$\frac{1}{V_p^2}\frac{\partial^2 P_D}{\partial t^2} + \nabla^2 P_D = S(x,t),\qquad\qquad 2.9$$

Residual P_λ wavefield is back-propagated in time axis using equation 2.9, but instead of using source S it uses $P^{obs} - P^{mod}$ (i.e. recorded shot gathers minus modelled shot gathers). In the first iteration when $P^{mod} = 0$, the output of equation 2.8 is the conventional RTM image. In next iterations, when we have the image I and the recorded seismic data P^{obs}, we can model P^{mod} by using acoustic wave equation as:

$$\frac{1}{V_p^2}\frac{\partial^2 P^{mod}}{\partial t^2} + \nabla^2 P^{mod} = P_D \cdot I,\qquad\qquad 2.10$$

Computed shots gathers P^{mod} allow to obtain a new residual wavefield P_λ, and then by equations 2.8 - 2.7 the subsurface image is updated. To define that the we get the optimum image, the misfit between recorded and modelled data is minimized in a least-squares sense:

$$S = \frac{1}{2}\left\| P^{obs}(x_r, t_{max}; s) - P^{mod}(x_r, t; s) \right\|,\qquad\qquad 2.8$$

In case of imaging first-order surface-related multiples, the source side wavefield P_D is replaced by the primary dataset and the recorded seismic data P^{obs} is replaced by the multiples dataset (ideally the first-order multiples only) which is produced by SRME.

2.5.   Full Wavefield Migration

The FWM method has been introduced and described in Berkhout (2014), Davydenko (2016), and more recently in Davydenko and Verschuur (2017). This method is very flexible and can be used to calculate different images: primaries, surface multiples, primaries and multiples together. In this study, we used FWM for producing the subsurface image from total reflection data, i.e. primaries, surface and internal multiples.

FWM makes use of two-way wave theory and is based on the wavefield relationship described in (Berkhout, 1982) The algorithm aims at minimizing the difference between the modelled and the recorded data by yielding subsurface reflectivity at every grid point of the subsurface. The estimated reflectivity is used to model the total reflection data by a finite-summation algorithm.

Multiple scattering and transmission effects are included (Berkhout, 2014). The residual (measured data minus modelled data) is imaged back to iteratively update the reflectivity.

The essential differences of FWM when comparing with other imaging methods is that it does not utilizes finite-difference modeling using standard parameters (velocity or density) but it explains seismic data by two independent operators, namely reflectivity R, transmission δT and propagation W. Together these operators are used in full-wavefield modeling (or FWMod). In this study, under the acoustic approximation we define δT as an approximation to R. The modeled data includes not just primaries but also higher-order scattering effects. FWMod recursively reconstruct primaries and multiples (order by order) (Davydenko, 2016).

At a depth level z_n, the wavefield can be described as the relation between the upgoing and downgoing wavefields from below and above the level z_n (Figure 2.5, superscripts $+/\cap$ and $-/\cup$ signs refer to down and upgoing wavefields, respectively). Scattering or secondary reflections are generated by using a scattering operator R_n, i.e reflectivity matrices and each element of this matrices define the reflectivity at a specific subsurface depth point. This scattering operator is determined from the estimated image. Each FWM iteration will update the image meaning that scattering operator will also updated. Wavefields are calculated for each depth interval Δz, between these small intervals the wavefield is propagated via the extrapolation operator W_n which is reconstructed from input velocity model. All operators are defined in the space-frequency domain (Berkhout, 1982).
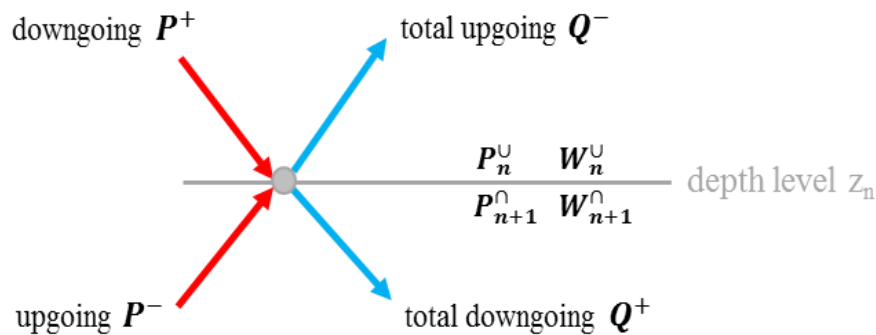
Figure 2.5: *Schematic diagram showing the full wavefield relation at depth level z_n (modified from Davydenko (2016))*

At each depth level, two incident or incoming wavefields (P^+, P^-), and two total (outgoing) wavefields (Q^+, Q^-) including scattering and transmission effects are computed (Figure 2.5). From the depth level z_n the total downgoing wavefields Q using operators W can be extrapolated to the next level $z_{n\mp 1}$ and becomes the incoming wavefields:

$$P^\pm = W(z_n, z_{n\mp 1})Q^\pm(z_{n\mp 1}).$$ <div style="text-align:right">2.12</div>

As mentioned earlier in case of the acoustic assumption we can approximate $\delta T^+ = R^\cup$ and $\delta T^- = R^\cap$. Then the total outgoing wavefield can be expressed as:

$$Q^+ = P^+(z_n) + R^\cup(z_n)P^+(z_n) + R^\cap(z_n)P^-(z_n)$$

$$Q^+ = P^+(z_n) + R^\cup(z_n)P^+(z_n) + R^\cap(z_n)P^-(z_n)$$ <div style="text-align:right">2.13</div>

The last terms in equations (2.13) can be represented as:

$$\delta S(z_n) = R^\cap(z_n)P^+(z_n) + R^\cap(z_n)P^-(z_n),$$ <div style="text-align:right">2.14</div>

where δS considered as the secondary sources at each depth level z_n. From equation (3), we can see that δS is defined as a linear relationship of the two incoming wavefields (P^+, P^-).

The FWMod process calculates the full wavefield at each depth interval, firstly estimating the outgoing wavefields:

$$Q^+(z_n) = P^+(z_n) + \delta S(z_n)$$

$$Q^-(z_n) = P^-(z_n) + \delta S(z_n),$$ <div style="text-align:right">2.15</div>

And then extrapolating the outgoing wavefield to the next level using the equation (2.12). By recursively applying the equations (2.15) and (2.12) the FWMod enables us to accumulate the downgoing incident wavefields:

$$P^+_{mod}(z_n) = \sum W(z_n, z_{n-1})\,[S^+(z_n) + \delta S(z_n)],$$ <div style="text-align:right">2.17</div>

After calculating the downgoing wavefield, we can update the secondary sources $\boldsymbol{\delta S}$ using equation (2.14). Note that, $\boldsymbol{P}^{+}_{mod}$ at depth $\boldsymbol{z_n = 0}$ is the recorded seismic data (i.e. $\boldsymbol{P}_{obs}(\boldsymbol{z_0})$) After that the upgoing incident wavefield computed:

$$\boldsymbol{P}^{-}_{mod}(\boldsymbol{z_n}) = \sum \boldsymbol{W}(\boldsymbol{z_n, z_{n+1}}) \, [\boldsymbol{S}^{-}(\boldsymbol{z_n}) + \boldsymbol{\delta S}(\boldsymbol{z_n})], \qquad 2.18$$

Given the velocity model, the FMW can be debrided as an inversion for updating the scattering operators $(\boldsymbol{R}^{\cup}, \boldsymbol{R}^{\cap})$ by minimizing the difference between observed data $\boldsymbol{P}_{obs}$ and modelled data $\boldsymbol{P}^{-}_{mod}$:

$$\boldsymbol{J}(\boldsymbol{R}^{\cup}\boldsymbol{R}^{\cap}) = \sum [\boldsymbol{P}_{obs}(\boldsymbol{z_0}) - \boldsymbol{P}^{-}_{mod}(\boldsymbol{z_0})] \qquad 2.19$$

More theoretical details provided by Berkhout (2014), Davydenko and Verschuur (2017).

3. Methodology

The methodology used in this study shown in Figure 3.1. It consists of the two main parts: velocity model building, and imaging with different reflection events.

First arrival traveltime tomography (FATT) and Full waveform inversion (FWI) were used as the main velocity analysis tools. The obtained velocity model is then used in the imaging process.

Least-squares reverse time migration is used for producing the images with primaries (LSRTM) and first-order surface-related multiples (LSMRTM). To separate primaries and surface-related multiples we have used the surface-related multiple elimination method (SRME). The full wavefield migration (FWM) algorithm is used to obtain the total reflection image. Throughout this thesis, by the total reflection we are referring to the primaries, surface-related and interval multiples together.

Before the actual imaging, preprocessing of the raw shot gathers is performed in order to prepare the input data for the imaging methods. The preprocessing flow consists mainly of muting the refraction waves and deghosting (i.e. removing the effect of receiver and source ghost reflections).
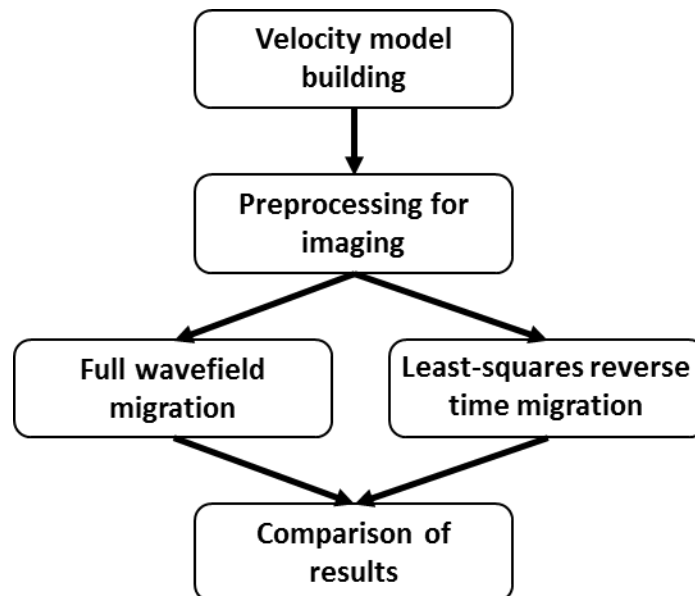
Figure 3.1: *Schematic diagram showing the main methods that were applied in this work.*

Velocity analysis, LSRTM and LSMRTM were implemented using the University of Stavanger in-house software Rockseis ® codes. FWM was done using the codes provided by the Delphi Consortium, Technical University of Delft. The minor processing steps related to data formatting, filtering and visualization were done using SeisSpace Promax ® and the open- source software Madagascar.

The above described methodology is applied to the 2D Chevron synthetic dataset and to the 2D broadband seismic datasets. The results of the implementation of the proposed methodology are discussed in Chapter 4 for the synthetic data, and in Chapter 5 for the field data.

3.1. First arrival traveltime tomography

In seismic imaging, a high resolution near-surface velocity model is very important to image correctly deeper structures. The FATT is a robust and computationally inexpensive algorithm for estimating near-surface velocities. Usually, this technique is used to obtain the initial velocities for pre-stack depth migration (Zhu et al., 2008). In this work, FATT was used to obtain the initial velocity field for the FWI.
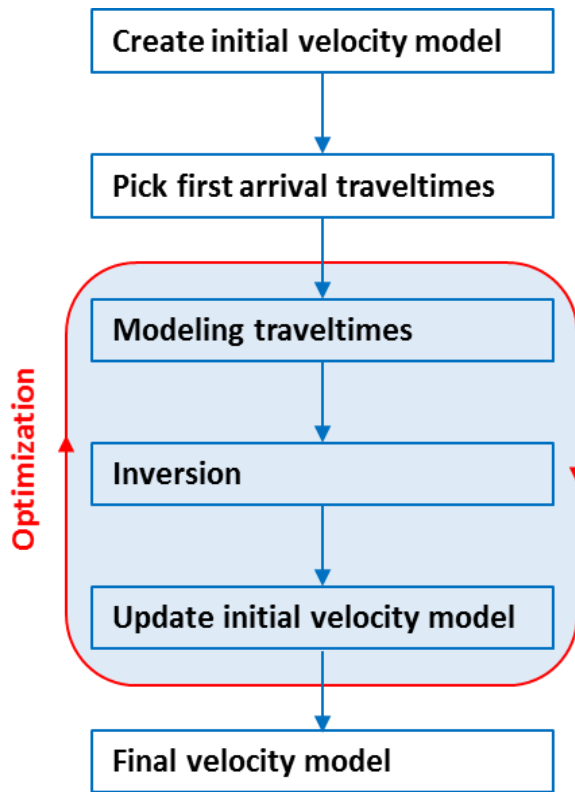
Figure 3.2: *Traveltime tomography workflow.*

The processing flow for the FATT is shown in Figure 3.2. Choosing the correct initial velocity model is an important and well-known issue for traveltime tomography. We started tomography for the field data with the velocity model obtained from conventional picking using a semblance of the velocity spectrum. The initial model for the synthetic data was provided as part of the dataset.

Using the shot gathers, the first breaks (i.e. traveltimes) of refracted waves were picked (Figure 3.3). The modelled traveltimes are subtracted from the picked traveltimes to produce an update to the initial model. Then the smoothed improved initial model was treated as a new initial model for the next iteration of tomography. This step is repeated until a good match between the modeled and observed traveltimes is obtained.
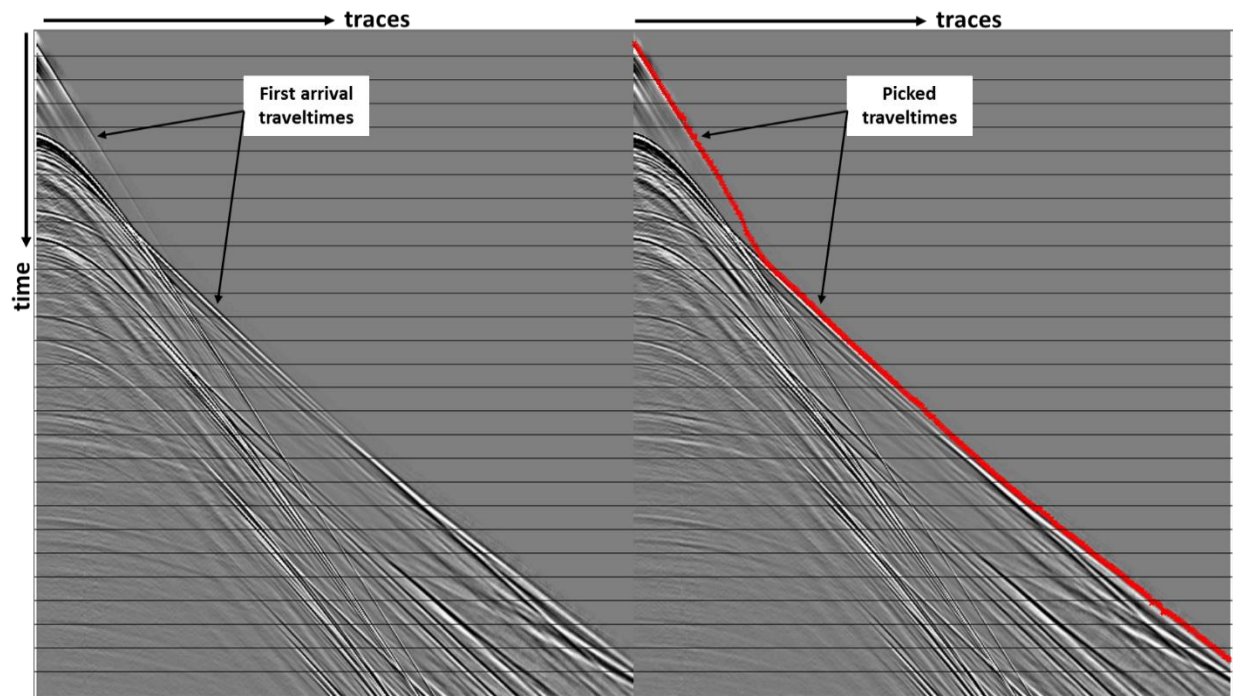
Figure 3.3: *Illustration of picking the first arrivals on the field data.*

3.2. Full waveform inversion

The FWI method is capable of providing an accurate and high-resolution velocity model, and most of the work of FWI is performed using the raw shot gathers without almost any preprocessing. The main steps of the data preparation for FWI include:

- Wavelet creation. The wavelet was provided in the case of the synthetic data (Figure 3.4a). For the field data, we first estimated a zero-phase wavelet based on the amplitude spectrum of the data. After that, we phase-corrected the estimated wavelet using a match filter obtained by matching the raw data and the shot gathers modelled with the zero-phase wavelet on the initial velocity model.

- In this study, we applied a multi-scale approach (Sirgue and Pratt, 2004). When running the FWI we used the data with the maximum frequency 15 Hz and 12.5 Hz for the synthetic and the field data, respectively. We started at 5 Hz and moved up by 2.5 Hz step. To create the datasets and the wavelets (Figure 3.4b) with the limited frequency bandwidth, we used a low-pass filter. Additionally, for the field data, the shot gathers were regularized from the 12.5x12.5 m grid to the new 20x20 m grid. It was done to increase the computational effectiveness.

- During the FWI, the velocity values at the water layer should not be updated. By applying a mute to the velocity updates, the velocities are updated only below the sea bed.
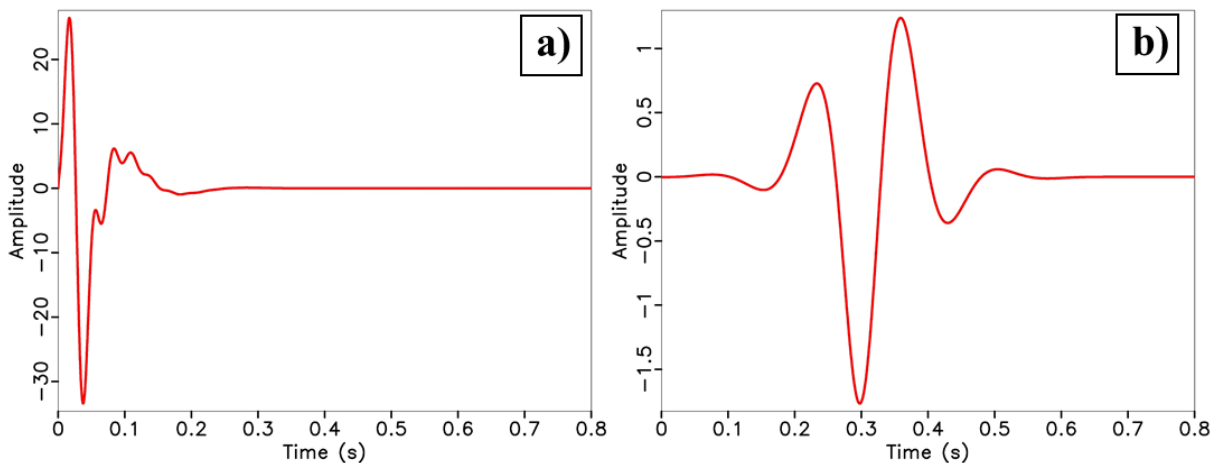
Figure 3.4: *(a) The original source wavelet and (b) the wavelet after low-pass filtering up to 5 Hz.*

- In the first iterations we used only refraction waves and the reflection events were muted by the inner muting function (Figure 3.5, marked by the red dashed line), the reflections were included only in the last iteration.
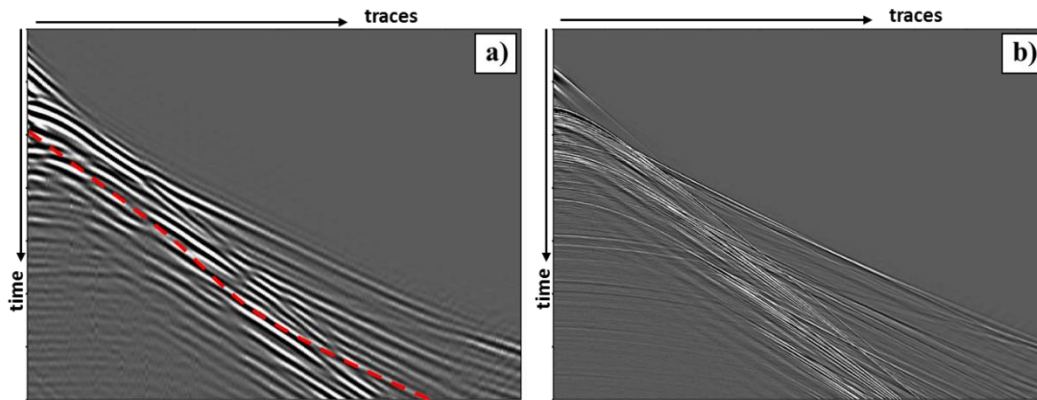
Figure 3.5: *(a) The regularized shot gather (20x20m) with maximum frequency 12.5Hz, (b) The original raw shot gather.*

The FWI consist of many iterations of the workflow shown in Figure 3.6. We can characterize the FWI as an iterative process between the reverse-time migration and velocity updating.

Firstly, the FWI workflow consist of calculating the modelled shot gathers using the initial velocity model and the density model (i.e. the velocity was converted to the density model by Gardner's law). Secondly, the gradient of the misfit between the raw and the modelled gathers is estimated. Thirdly, the estimated gradient is imaged by cross-correlating the source wavefield and the backward modelled residual wavefield. Finally, the obtained image provides the velocity updates which are added to the initial velocity model. Then, a new iteration of FWI starts with the updated velocities.
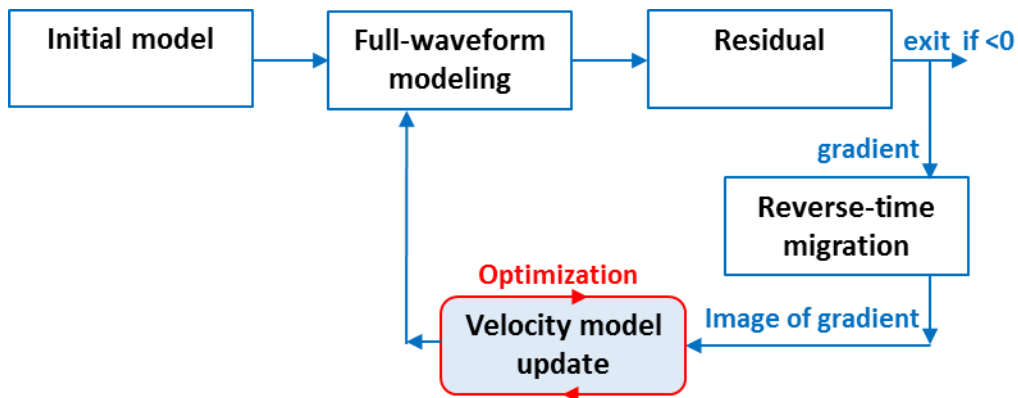
Figure 3.6: *Schematic diagram of the FWI workflow*

3.3. Preprocessing

Before the actual imaging, we should prepare the shot gathers removing undesired seismic event, which are not supposed to be imaged. The preprocessing includes removing direct and refraction waves by muting, deghosting and SRME.

The main reason for application of the deghosting algorithm is to remove the effect of source and receiver ghosts and to increase resolution (Ikelle and Amundsen, 2005). Figure 3.7 demonstrates the results of deghosting. Note that, after deghosting the seismic data is redatumed to the free surface level. It means that all the images will be referenced to the free surface, i.e. zero level.

For the LSRTM and LSMRTM the input shot gathers were created by using SRME. The output of SRME is the primary dataset, then the subtraction of the primaries from the deghosted shot gathers provides the surface-related multiple dataset for the LSMRTM.

In FWM methods, as an input data we used the shot gathers after muting the refraction events and the deghosting. Note that, we did not apply any multiple elimination algorithms to the input data of the FWM.
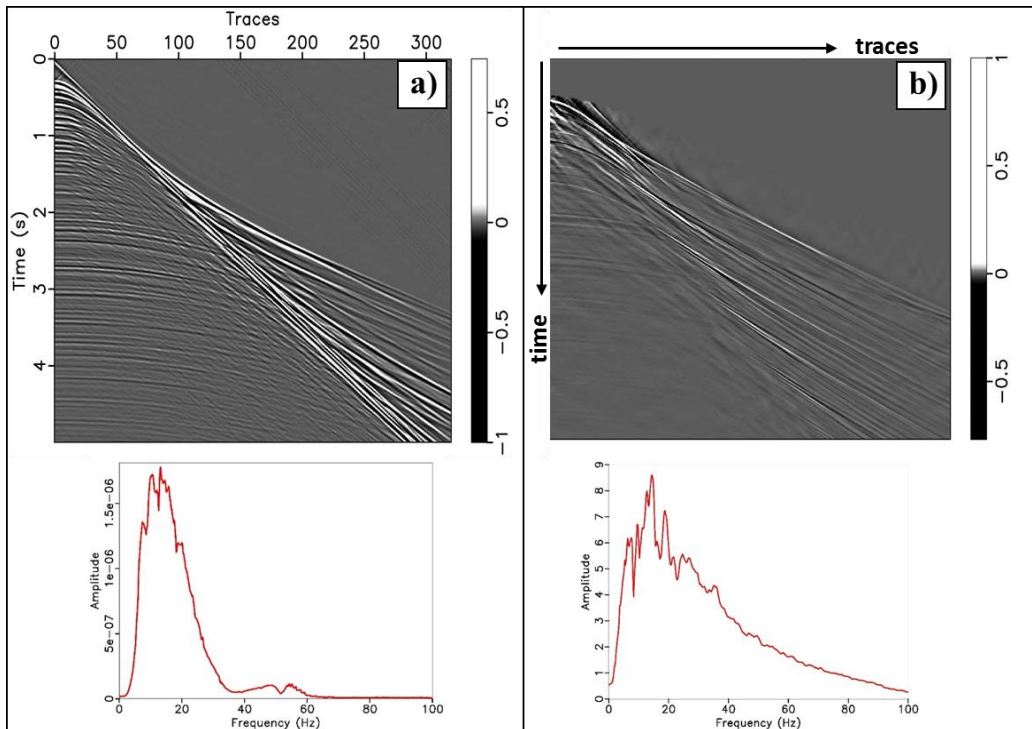
Figure 3.7: *Shot gathers and their amplitude spectrums after deghosting: (a) synthetic data, (b) filed data*

3.4. Least-squares reverse time migration

The source wavelets used in LSRTM method are shown Figure 3.8. Taken into account the frequency bandwidths of the synthetic and the field data after deghosting, as well as the computational resources, the maximum frequencies for migration were chosen. We decided to use the maximum frequency of 40 Hz for the synthetic data, and 60 Hz for field data (Figure 3.8).

Figure 3.9 shows the least-squares imaging approach (Weibull and Arntsen, 2014) with primaries. The input datasets consist of: the velocity model after FWI, the constant density model, the primary dataset after SRME.

The first iteration of LSRTM is similar to the conventional RTM approach, the image is produced by cross-correlating the source side wavefield with receiver side wavefield. In the next iteration, the upgoing receiver wavefield is modeled as the residual between the observed and the modeled shot gathers. The modeled shot gathers are calculated by taking into account the image from the first iteration. The cross-correlation of the forward propagated source wavefield with the back-propagated residual receiver wavefield produces the image update. This image update is added to the image from the first iteration. After that, a new iteration of LSRTM starts.
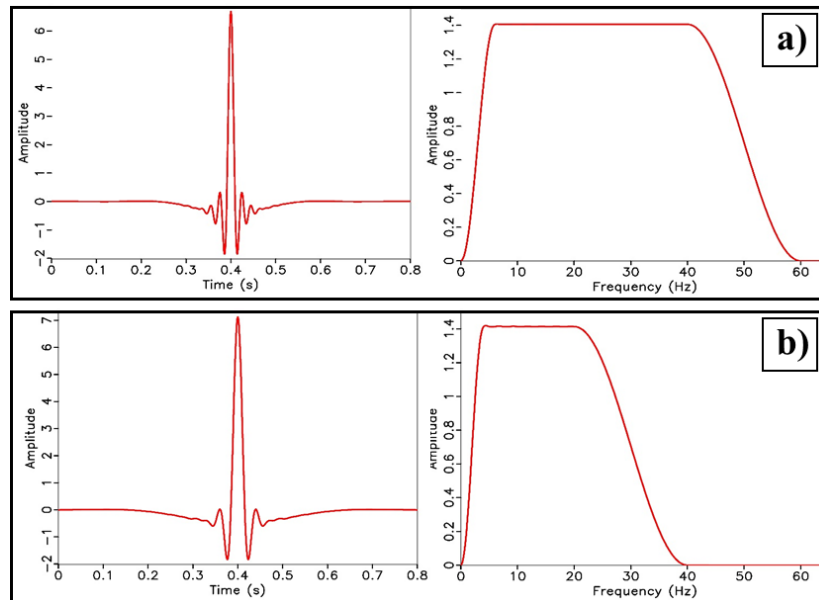
Figure 3.8: *Tukey wavelet and its amplitude spectrum used in the LSRTM: (a) field data () synthetic data*

Figure 3.9b shows the differences between the LSRTM and LSMRTM methods. As we can see, in LSMRTM source wavefield is replaced by forward propagated primaries multiplied by -1, and the residual receiver wavefield is replaced by surface-related multiple dataset. The residual wavefield is estimated as the difference between the input (i.e. observed) and the modeled surface-related multiples. Note that, in LSRTM, the source is equivalent to a point, while in LSMRTM the free surface becomes the source surface.
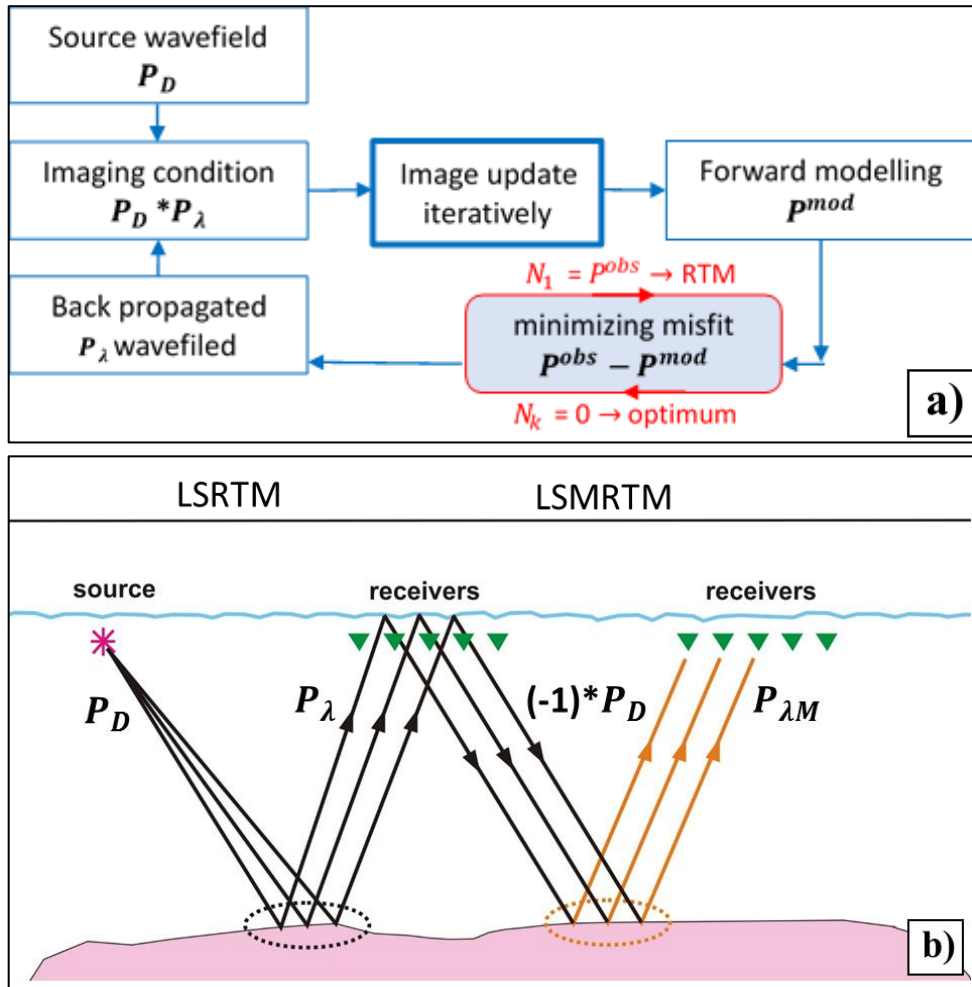
Figure 3.9: *(a) A general scheme of the LSRTM, (b) Schematic diagram showing the principle of imaging with primaries and first-order surface multipl.*

3.5. Full wavefield migration

The most important characteristics of FWM method are:

- Inversion based algorithm in terms of reflectivity;
- Assumes that the velocity is defined prior to migration;
- Multiples not removed from the input shot gathers;
- The algorithm can handle all surface-related and internal multiples;
- Can be applied in the different mode (total data, primaries, surface-related multiples).

In FWM imaging with total reflection data, the source side wavefield is the forward propagated recorded data with the source wavelet, and the receiver side wavefield is the back-propagated data after deghosting. The first iteration is similar to RTM. The estimated image after the first iteration provides a reflectivity update. Note that, FWMod models all orders of surface-related and internal multiples in the first iteration. In the next iteration, a new wavefield produced by FWMod taking into account the updated reflectivity. The modelled upgoing (incident) wavefield compared with the recorded data, and the difference imaged in the next iteration producing the new reflectivity update. Each iteration of FWM enable us to remove the multiple crosstalks due to the improved reflectivity model.
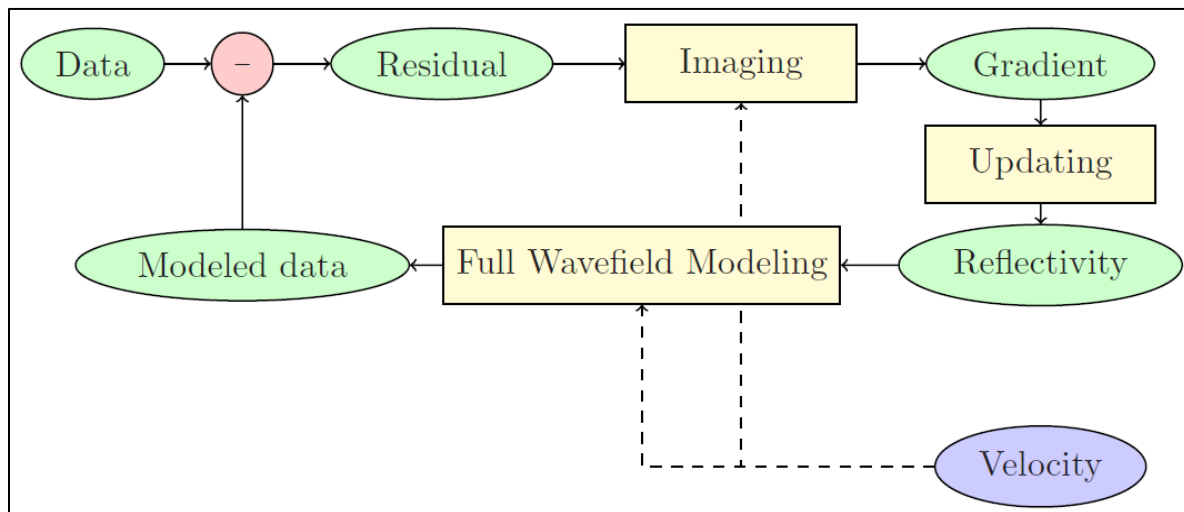
Figure 3.10: *The general scheme of FWM (Davydenko and Verschuur, 2017).*

4.   Synthetic data application

We applied the proposed methodology to the 2D Chevron marine synthetic data. This synthetic dataset is modelled as an isotropic elastic wavefield under a 2D earth assumption. A seismic line 48 km along, which corresponds to 1600 shots was used. The main seismic parameters are described in Table 4.1.

Table 4.1: *Data specifications*

Source point interval, m	25
Source depth, m	15
Streamer length, m	8000
Receiver interval, m	25
Receiver depth, m	15
Sample rate, ms	4
Record length, sec.	8
Channels per streamer	321
Number of shot gathers	1600
Max offset, m	8025
Min offset, m	25
Fold	160
Line length, km	48

The Chevron synthetic data was designed as a blind data test, meaning that the original model parameters (density, velocity, etc.) are not provided. The data consist of raw shot gathers, an initial velocity model, well log velocity information and a ghost free wavelet. resem

4.1. Velocity model building

In this section, we demonstrate the improvement of the initial velocity model using FATT and FWI. As noted earlier, inaccurate velocities lead to poor imaging (i.e. misfocusing reflectors, artifacts, wrong depths). Even though velocity model building is not the main objective in this study, we need accurate high-resolution velocity models in order to get a good quality seismic images with the RTM and FWM methods (Jones, 2010).

The initial velocity model is heavily smooth (Figure 4.1). It was provided as a part of the Chevron synthetic dataset. The model dimensions are 48 km horizontally and 5 km in depth. Using the velocity gradient, we can recognize three different zones. From the seabed to 1.9 km, velocity increases gradually from 1500 m/s to 3600 m/s. It is nearly constant, around 3600 m/s, from 1.9 km to 2.4 km, and then we can observe velocity inversion around 2.6 km depth where velocity changes from 3600 m/s to 3200 m/s. This velocity decrease indicates the presence of strong multiple-generator reflectors in this depth level. Then from 2.7 km to 5 km velocity increases steadily from 3200 m/s to 4100 m/s.
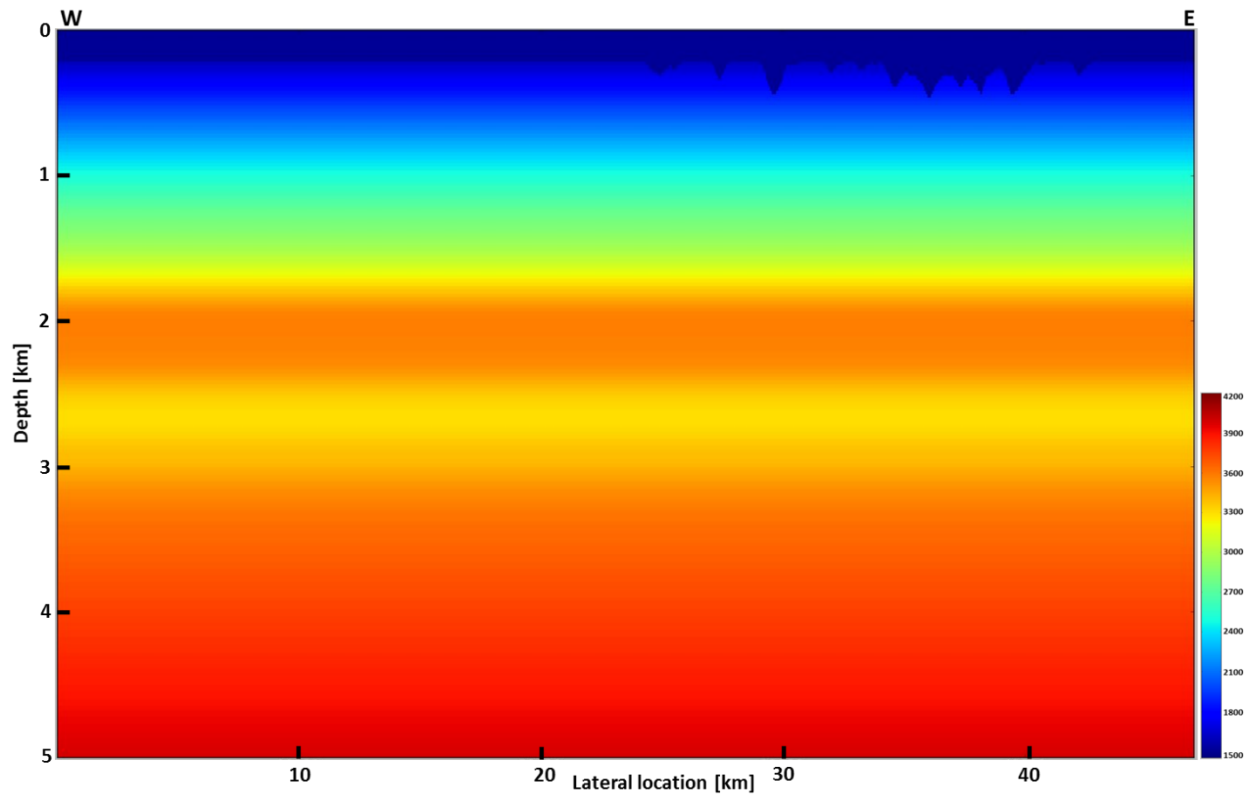
Figure 4.1: *Initial velocity model.*

Figure 4.3a shows the velocity model after the FATT. We can see that tomography improved the velocity distribution from seabed down to about 2 km. In between these depths, the velocity structure is clearly more laterally variable. The updated model enables us to see some major structural features (Figure 4.3a). For examples, up to 0.8 km velocity has continuous coherent structure. Below seabed there are several low-velocity circled anomalies (between 10 - 20 km horizontally). Sharp contrast boundary around 1.7 - 1.8 km velocity structure with irregular geometry highlighted. There is a slight dipping of near-surface velocity structure (up 1.9 km) towards east direction.

Figure 4.3b demonstrates the differences between updated and initial models. The eastern part of the model mainly decreased by 60 - 220 m/s, meanwhile the western part increased by 100 - 250 m/s. Having 8 km offset limit, and due to a high velocity layer, tomography was limited to updating the near-surface velocity field.

After updating velocities, we need to confirm that the obtained model is reasonable, i.e. it explains the seismic data and makes geological sense. The quality control procedure for FATT consist of comparing the predicted and observed traveltimes. Figure 4.2 shows such a comparison, where we can see a good match between the modeled and the picked traveltimes.
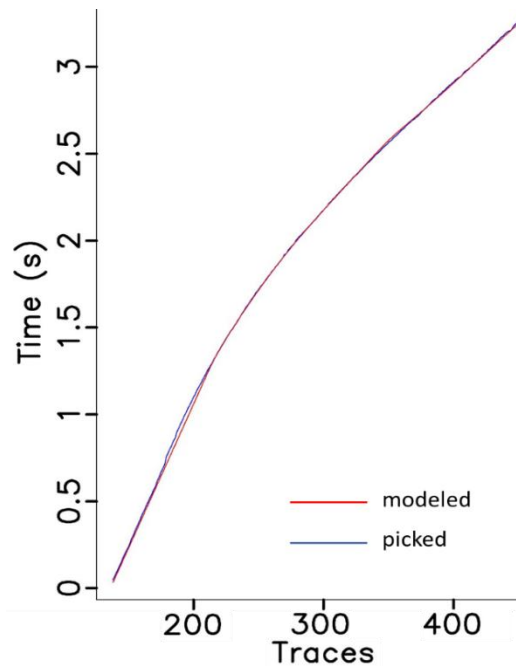
Figure 4.2: *Comparison of traveltimes for a single shot.*
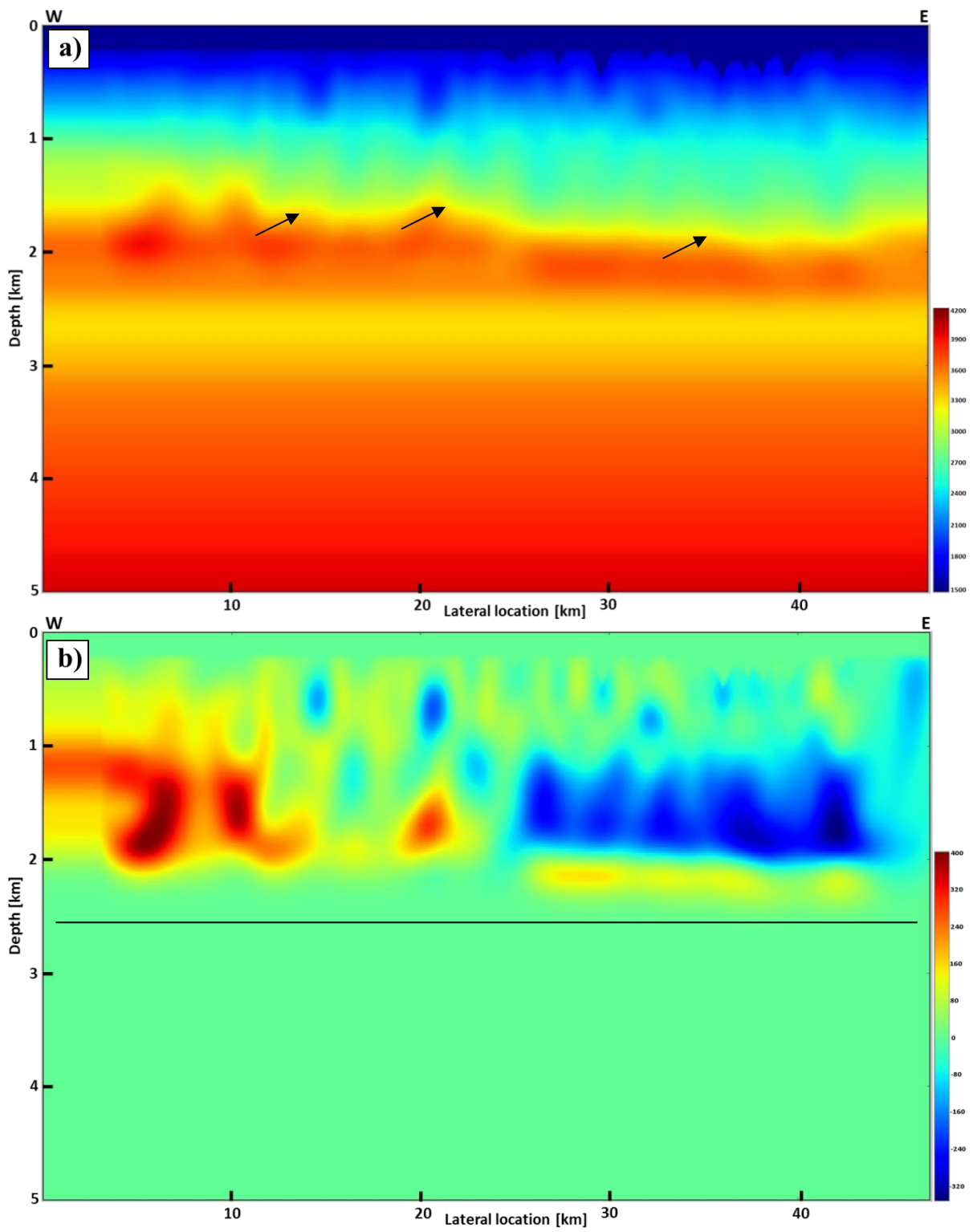
Figure 4.3: (a) Tomography model, (b) velocity updates after tomography.

The velocity model after FWI is shown in Figure 4.4a. We can clearly see that FWI highlighted not just the smooth geological trend with specific direction but also deeper and finer details of the velocity field. Figure 4.4b shows the ability of FWI to update the velocity model below the tomography penetration limit that is around 2 km as shown in Figure 4.3b. Comparison of FATT (Figure 4.3a) and FWI (figure 4.4a) results demonstrates some parallelism related to geological trend within data. The possibility of seeing reflection events on the FWI model down at around 4 km indicates that some reflection information was used in the FWI procedure (Figure 4.3a). Note that below 4 km velocities does not improve due limitations of FWI to penetrate deeper (Virieux and Operto, 2009).

The FWI velocity model can be divided into three depth zones. Zone I consist of a water layer and shallow sediments with velocities 1450 m/s – 2100 m/s. We see the shallow gas anomalies circled in black in Figure 4.4b. Due to a notable velocity changes within this zone, we can observe some layering. Zone II is characterized by high-velocity channels with steep dips and complex shapes. One main advantage of FWI compared to conventional semblance based velocity analysis is that it can correctly incorporate such high contrast anomalies with complex geometry into the velocity model (Virieux and Operto, 2009). Usually, when such channel anomalies in the velocity field are picked up incorrectly, they cause pull-up and push down effects leading to image distortion in depth migration (Yilmaz, 2001). Another characteristic of zone II is the absence of evident continuous reflectors, the velocity changes are very smooth within the zone.

The velocity changes in zone III resemble the subsurface image, the enhancement brought by FWI indicates the change in reflectivity (i.e. constrasts in the acoustic impedance, or density multiplied to velocity) and it is consistent with the geometry of the reflectors. This zone contains relatively simple structures, reflectors are mainly flat and with increase in depth. The geometry of reflectors can be associated with an anticline structure. Velocity variation is mainly observed in the vertical direction with strong notable decrease from 3600 m/s to 3200 m/s at 2.7 km. Figure 4.4b demonstrates lateral velocity changes 50 - 100 m/s within this zone which show the presence of small heterogeneity.

The quality control procedure for FWI consisted of comparison of modeled and observed seismic datasets, i.e. checking the presence of cycle skipping problems (Sirgue and Pratt, 2004). In each

FWI iteration the output synthetic shot gathers were compared to observed data to make sure that a good correlation between these gathers and velocity updates corresponded to a meaningful geological trend.
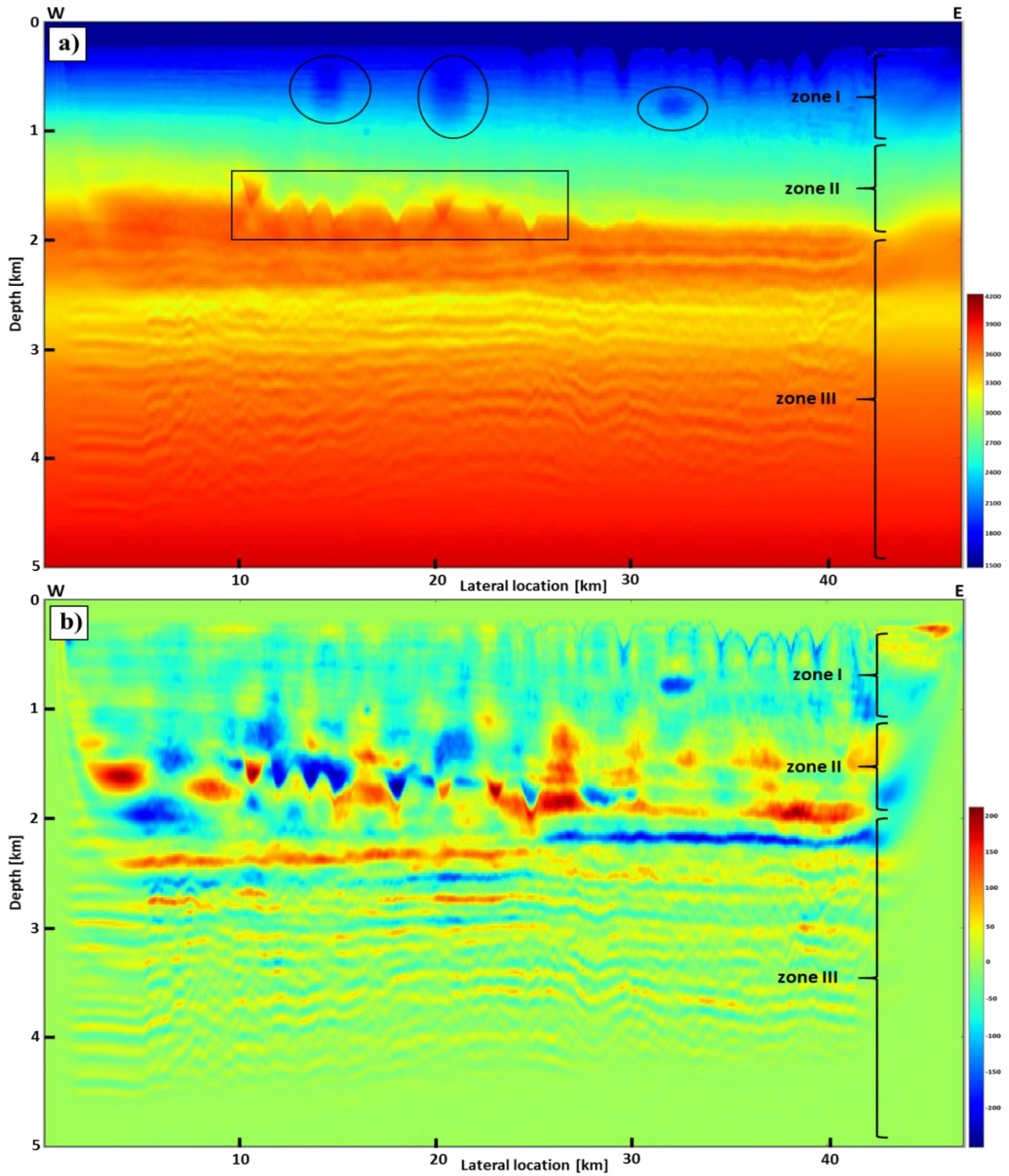
Figure 4.4: *(a) FWI model, (b) velocity updates after FWI.*

4.2.   Preprocessing for imaging

In this section, we discuss the processing steps before imaging. Conventional processing of data aims to eliminate all kind of seismic events except the primary reflections, i.e. to improve signal-to-noise ratio (Yilmaz, 2001). In this study, processing was used not to discard the multiples, but to separate them from the primary dataset. Before actual imaging, shot gathers should be preprocessed. The preprocessing includes removing direct and refracted waves by muting, deghosting and SRME.

The raw shot gather (Figure 4.5a) consists mainly of reflection and refraction events. Reflection waves show strong periodicity, especially in the shallow part. We can also note the absence of random noise in the data. Refraction events are characterized by stronger amplitudes, low frequencies and they mask reflections at far offsets (Figure 4.5a). The result of deghosting is demonstrated in Figure 4.5b, where reflection events become compressed (i.e. increase of resolution). Figure 4.5c display the results of muting, refraction is surgically removed and only reflection are left. The results after muting are used as input for SRME for separating primaries from surface-related multiples.
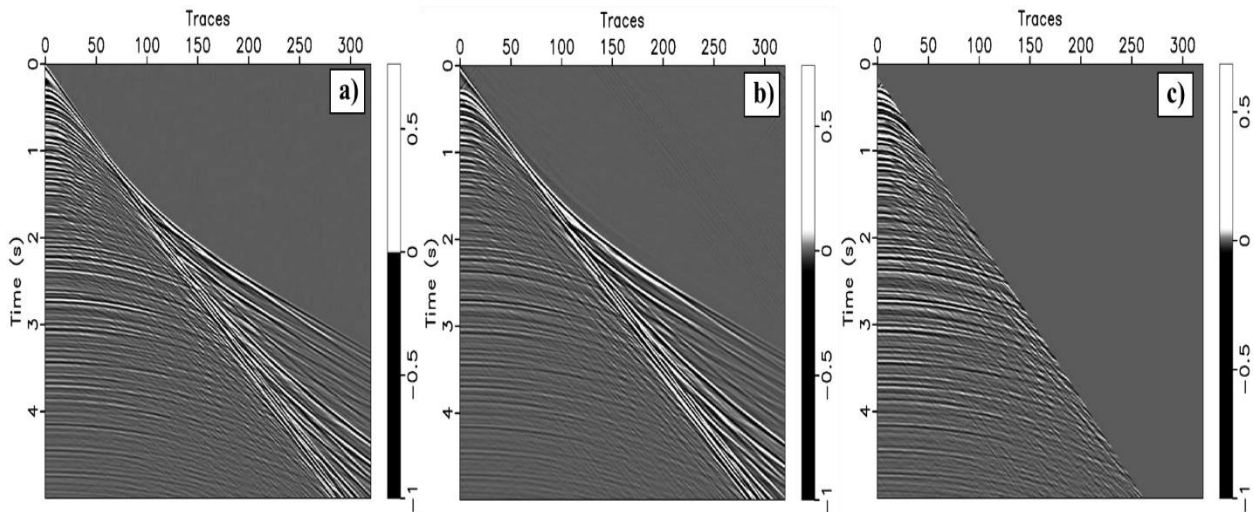
Figure 4.5: *Shot gathers: raw (a), after deghosting (b), after muting (c).*

Figure 4.6a displays common offset gather (975m.). The offset is defined as the distance from source to receiver. The sea bottom is at about 0.3 sec. In the upper part (Figure 4.6a) we can clearly see strong surface multiples, indicated by arrows. Surface multiple related to water bottom (indicated by red arrows) repeats the water bottom topography. Around 1.8 sec, we can see surface multiples with V-shape geometry (indicated by yellow arrows) which originated from channel type events at 1.5 sec. Strong subsurface reflectors in between 2 - 3 sec, generate their own surface multiples (highlighted by the red rectangle). There are some reverberations related to a group of reflectors from 0.8 - 1.2 sec and 2.3 - 2.7 sec. observed in the western part.

The result of SRME are shown in Figure 4.6b. We can see how surface multiples are removed, strong multiples related to sea bed (red arrows) are well eliminated. Multiples from channel type reflectors at 1.5 sec (yellow arrows) are also very well removed and we can see more clearly the primaries which were previously masked.

Subtraction of predicted multiples in SRME does not always work perfectly (Dragoset et al., 2010). An example is shown on Figure 4.6b where, primary reflectors in the area highlighted by the red rectangle are slightly damaged by SRME. This means that multiples have very close properties to the primaries and interfere with them in such way that removing multiples will lead to the damage of primary reflections. Besides , there can be some residual multiple energy left, even if we cannot discriminate them on the common offset gathers. However, they clearly can identified after migration.
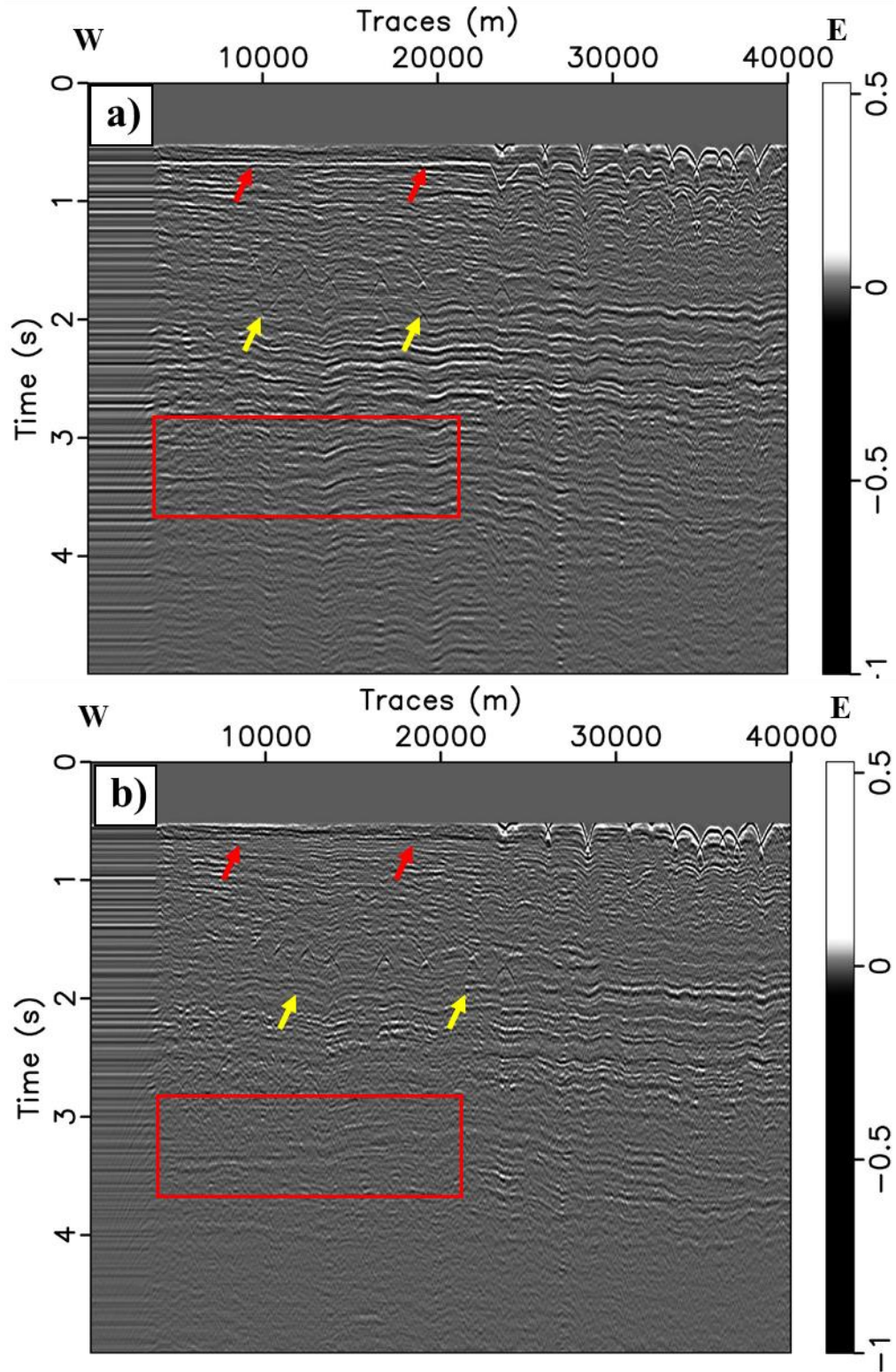
Figure 4.6: *Common offset gather showing data (a) before and (b) after SRME.*

4.3. Imaging

This section contains the imaging results of the Chevron synthetic data after LSRTM imaging with primaries, after LSMRTM imaging with first-order surface multiples, and after FWM imaging with the total reflection data, i.e. primaries, surface-related and internal multiples. In the next section, we will perform a comparison between the implemented imaging methods and define advantages and limitations of these methods within the Chevron synthetic data.

Figure 4.7 illustrates the three shot gathers which were used in the imaging process. Note that, multiple shot gathers (Figure 4.7c) obtained after SRME consist of first-order surface multiples as well as higher order multiples. In this work, our RTM methods assume that the multiple dataset contains only first-order surface multiples, so the other orders of surface-related multiples may cause negative effects on the images.
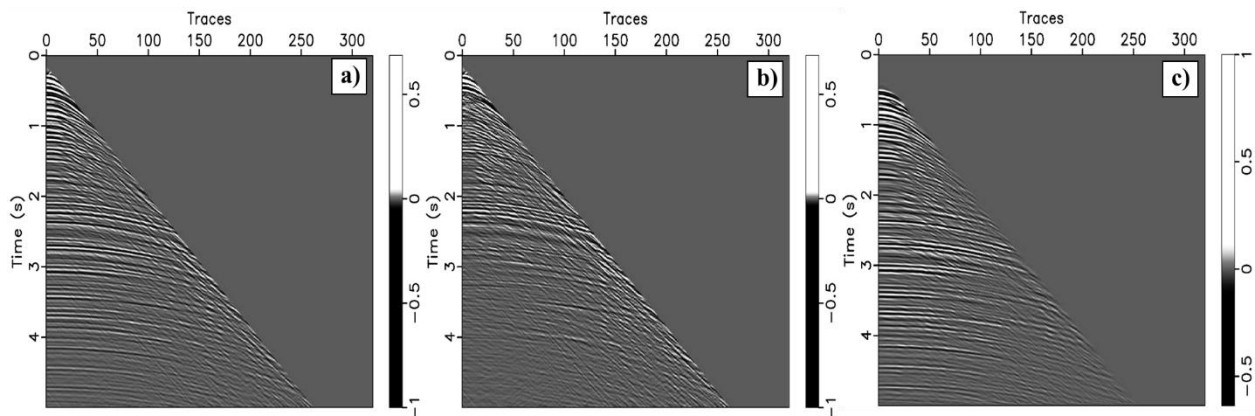
Figure 4.7: *Total reflection data (a), primaries (b) and surface multiples (c).*

Figure 4.8 compares the stacks derived from LSRTM imaging with primaries. The image at first iteration (Figure 4.8a) represent standard reverse-time migration image. The final LSRTM image was obtained after the iterations 9 (Figure 4.8b). The poor amplitudes in the first iteration are due to the amplitude-gain procedure, which was not applied in the preprocessing. In a conventional processing sequence, special gain functions and amplitude scaling algorithms are applied to get true amplitudes (Yilmaz, 2001). In this work we focused mostly on structural imaging rather than in amplitude processing. Amplitudes are improved by applying the least-squares approach and are also scaled globally (i.e.-1 to 1) in all results to match phase differences.

The final LSRTM image is shown in Figure 4.8b. It is clearly visible that the image is more focused in terms of amplitudes and have a broader frequency spectrum. Weak low-frequency artifacts (indicated by the red arrows) could be observed at 0.5 km which can be explained by remaining residuals of strong first-order surface multiples. We can see identifiable continuous reflectors in the entire section, and gently dipping reflectors can be seen up at around 5.5 km. That gives us confidence that velocity model in migration was correct. Usually, in case of velocity errors, the output image will contain migration 'smiles', especially in the deeper parts (Yilmaz, 2001). The primary image does not show any conflicting crossing events or crosstalk (i.e. multiple reflection energy which is not separated from primaries).

The image in the shallow part (0 - 1.1 km) has poorer resolution, reflectors disappear and are more difficult to correlate laterally. In the area indicated by the red rectangle (Figure 4.8b) some reflectors (3.6 - 3.8 km) and are distorted. This can be explained by the complex geological settings within this part of the section and by the strong multiple elimination, which distorted primaries. The channel feature type events at 1.5 km are well imaged, and their reflector boundaries illuminated accurately.

At around 30 km lateral position and 3km depth, we can identify a small scale low velocity anomaly circled in yellow which causes sagging (i.e. push down effect) in the deep structures (Figure 4.8b, indicated by the yellow arrows). This effect could potentially be corrected using reflection tomography (Jones, 2010), however this methodology was out of the scope of this thesis.

The results of LSMRTM imaging with first order surface multiples at the first iteration and after the iteration 7 are shown in Figure 4.9a and Figure 4.9b, respectively. The image also has improved in terms of amplitudes of the primary events. Moreover, the sharpening effect of least-squares approach more is more recognizable, especially at shallow depths. The artifact from second order surface multiples can be seen in Figure 4.9 indicated by red arrows. As we mentioned earlier, the output of SRME contain all possible order of surface-related multiples. However, our imaging method, assume that all surface-related multiples are first order. To remove this artifact related to higher order multiples it is possible to extend the SRME methodology in such way that it can predict and subtract only first order surface multiples (Verschuur, 1991). However, in this thesis we did not consider such an approach.
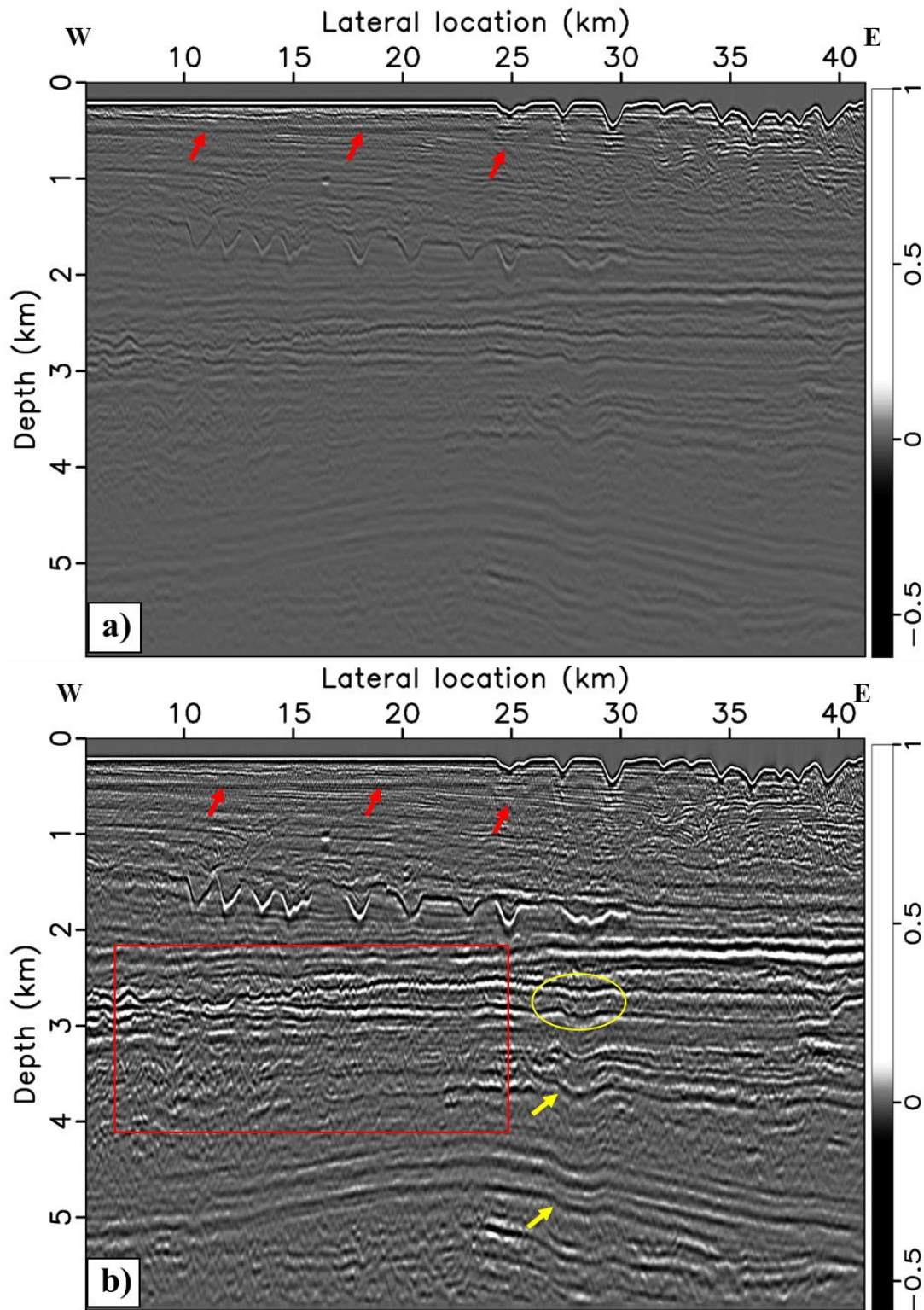
Figure 4.8: *Comparison of LSRTM imaging with primaries: (a) image at the first iteration; (b) image at the 7ᵗʰ iteration.*
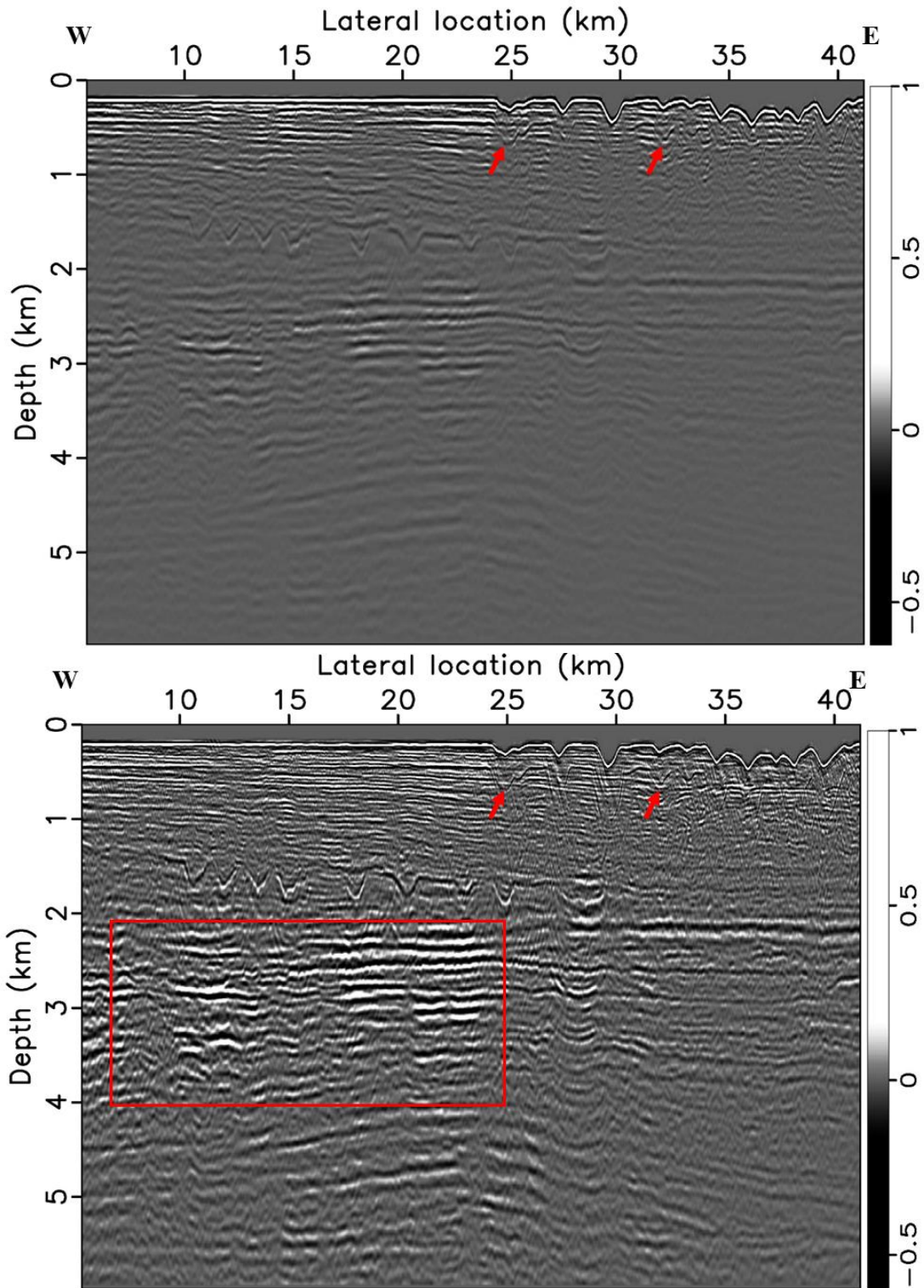
Figure 4.9: *Comparison of LSMRTM imaging with surface-related multiples: (a) image at the first iteration; (b) image at the 7th iteration.*

Reflectors at around 2 - 5 km highlighted by the red rectangle have strong amplitudes. This strong amplitude anomaly zone could be explained by a high velocity contrast related to the unconformity surface (Figure 4.4), which generates strong multiple reverberations of surface-related multiples and also internal multiples. That means this area is complicated mainly due to the interference between different reflection events including higher order multiples. Hence, the first order surface-related multiple image is less reliable in that depth range due to the presence of artifacts from higher order surface-related and internal multiples.

It is noticeable that below 4 km depth, the first order surface multiple image is poorly illuminated and reflectors are not easily detectible (Figure 4.9b). This is reasonable since the primary reflectors from such depth are weak and barely recorded at the receivers while their multiples will be even weaker. It means that information coming from surface multiples are not sufficient enough for proper subsurface illumination of deep structures.

From the sea bed down to 1.2 km depth (Figure 4.9b) we can clearly see the added value of first order surface multiple illumination, reflectors are identifiable and continuous. The reflection configuration consists of thin layering within this shallow depth. In practice, using primaries to interpret such fine details at shallow depth is impossible due to poor source sampling and bad angle coverage of primaries (Lu et al., 2014). However, as we can see from Figure 4.9b that incorporating surface-related multiple enhance shallow image making it more geologically interpretable.
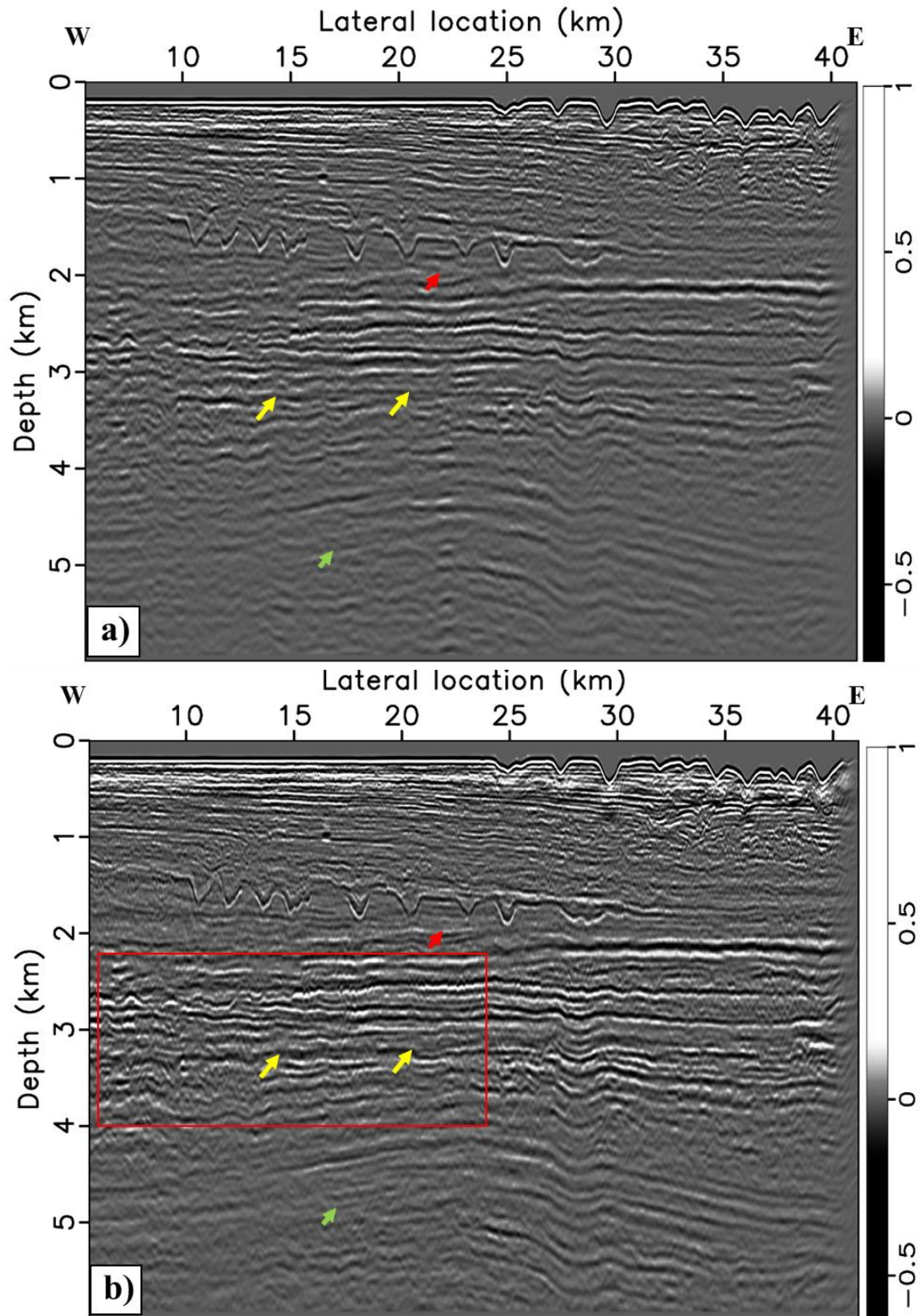
Figure 4.10: *Comparison of FWM imaging with total data: (a) image at the first iteration; (b) image at the 15th iteration.*

4.4. Comparison of results

Next, we show a comparison of results of LSRTM, LSMRTM and FWM. Note that, by surface-related multiple image we refer to the first-order surface-related multiple image.

Before the actual comparison, as a quality control procedure we compared produced images with the spatial vertical derivative of the velocity model (Figure 4.11) after FWI (Figure 4.4a) which was used in the depth migration process. When we incorporate reflections into the FWI process, the output velocity model is kinematically equivalent to a migrated image (Sirgue and Pratt, 2004). Taking a vertical derivative corresponds to a filtering process which will increase the resolution of the input data (Yilmaz, 2001). We can see that the vertical derivative of the velocity (Figure 4.11) is close to a subsurface reflectivity image with the predominant influence of the low-frequencies where the main reflectors clearly observable. We compared imaging results (Figure 4.8a, 4.9b, 4.10b) with the vertical derivative of the velocity (Figure 4.11) and find that imaging algorithms honored quite well the velocity model. Indeed, main reflectors in the images match in depth with the velocity model.
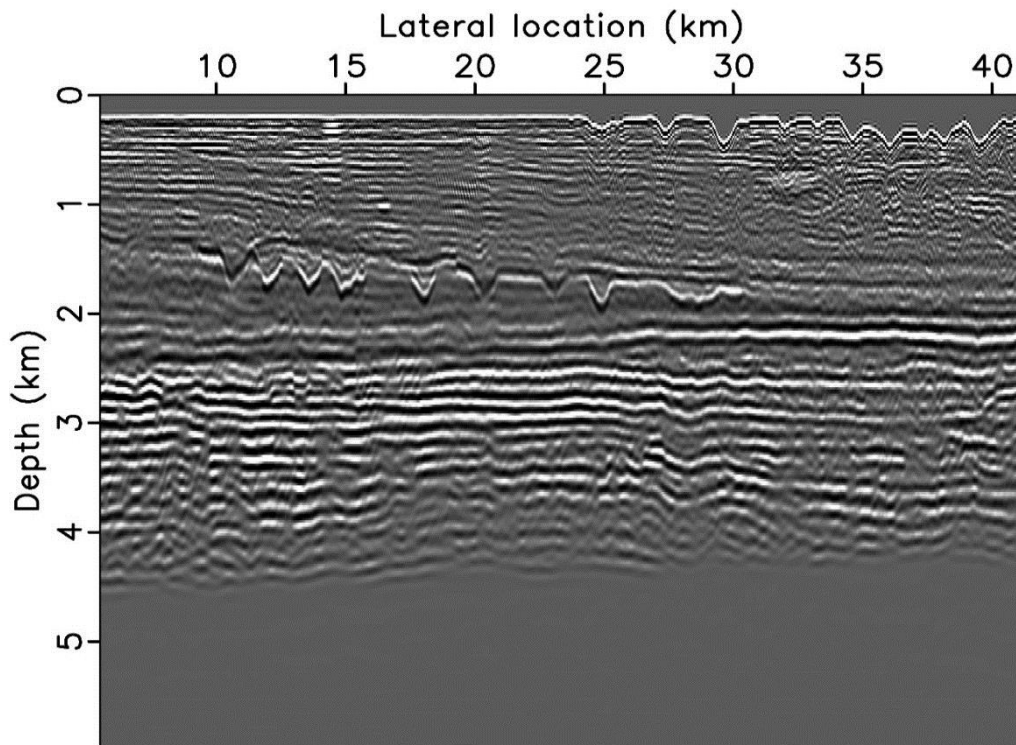
Figure 4.11: *Vertical derivative of the velocity model after FWI.*

It is interesting to remark that the penetration depth of FWI is around 4.5 km. It means that our velocity model was not improved below 4.5 km and that the images below that depth are less reliable.

Figure 4.12 compares the images produced by LSRTM primary imaging (Figure 4.11a), LSMRTM first-order surface-related multiple imaging (Figure 4.12b) and FWM total reflection data imaging (Figure 4.12c). We can clearly recognize the contribution of multiples to enhance the images at shallow depths. Reflectors located between 0 - 20 km laterally and up to 0.5 km depth are better imaged (indicated by red arrows), we can see a cleaner differentiation between reflectors. LSMRTM image has a better image of small features when compared with FWM. As discussed earlier, the surface-related multiples have more narrow reflection angles and lead to some limitations when imaging steeply dipping events, such as the channel type events at around 1.8 km depth (Figure 4.12b). It mean that that information coming from surface-related multiples cannot replace the contribution from the primaries.
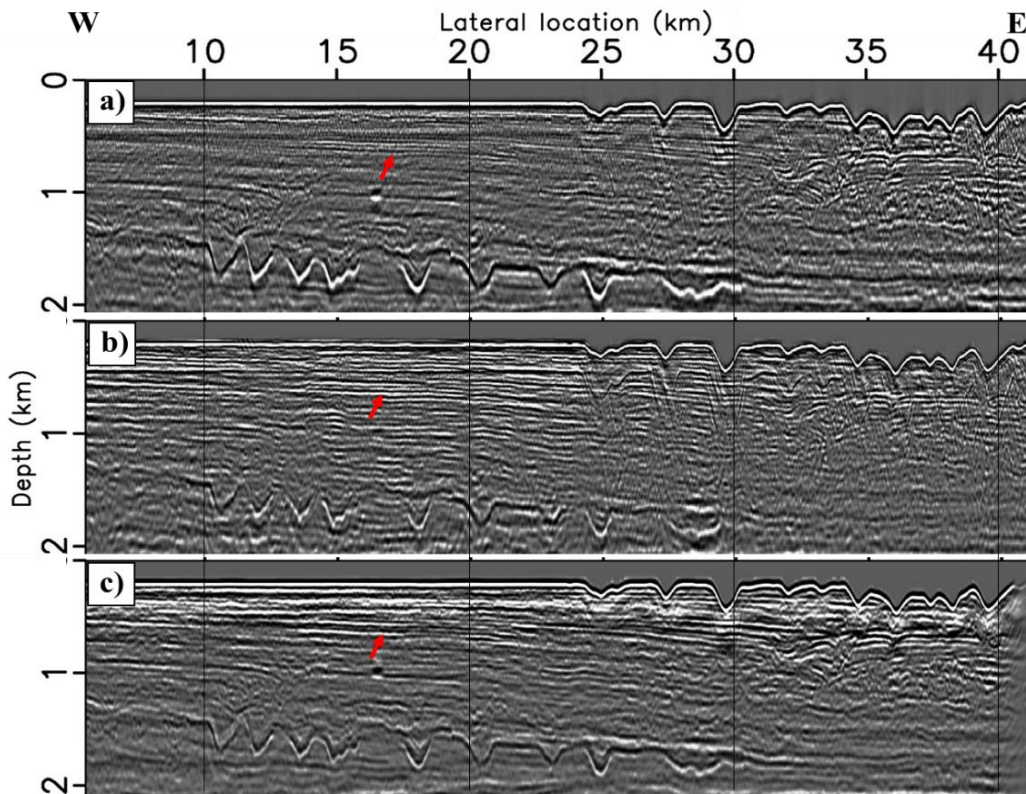
Figure 4.12: *Comparison of (a) LSRTM primary image, (b) LSMRTM surface multiple image and (c) FWM total image. The images are zoomed between 0 - 2 km depths.*

It is noticeable that between 0 - 2 km depths, the FWM image is much more interpretable. The geometry of the reflectors has better lateral continuity (Figure 4.12b).

Next, we compare the images in between 2 - 4 km depths. As we discussed previously in section 4.1, this depth interval is characterized by velocity inversion. The velocity values change from 3600 m/s to 3200 m/s and we relate this zone to a strong internal multiple generator. Indeed, if we look at the primary image (Figure 4.13a) and first-order surface-related multiples image (Figure 4.13b), both of them have poor illumination, especially in areas highlighted by the blue crosses. In the primary image we separated multiples and therefore we cannot see many artifacts, while the

Figure 4.13: *Comparison of LSRTM primary image (a), LSMRTM surface multiple image and (c) FWM total image. The images are zoomed in between 2 - 4 km depths.*

surface-related multiple image is contaminated by crosstalk from higher-order multiples (i.e. LSMRTM properly images only the first-order surface-related multiples). However, in the total reflection image (Figure 4.13c), the improvement of the illumination is clearly visible.

For example, observe the reflectors indicated by the red arrows, which are invisible in the primary image and misfocused in the first order surface multiple image, while in the total reflection image, these reflectors are identifiable. For the depth interval 2 - 4 km FWM with the total reflection data produces a better image of small features and we can more easily differentiate reflectors, when compared with the primary and the surface-related multiples (Figure 4.13c).

Figure 4.14 shows a comparison of the imaging of the deepest reflectors. Continuity of reflectors is most notable in the primary image (indicated by red arrows). Note that the internal multiples bring some details (indicated by the yellow arrows).
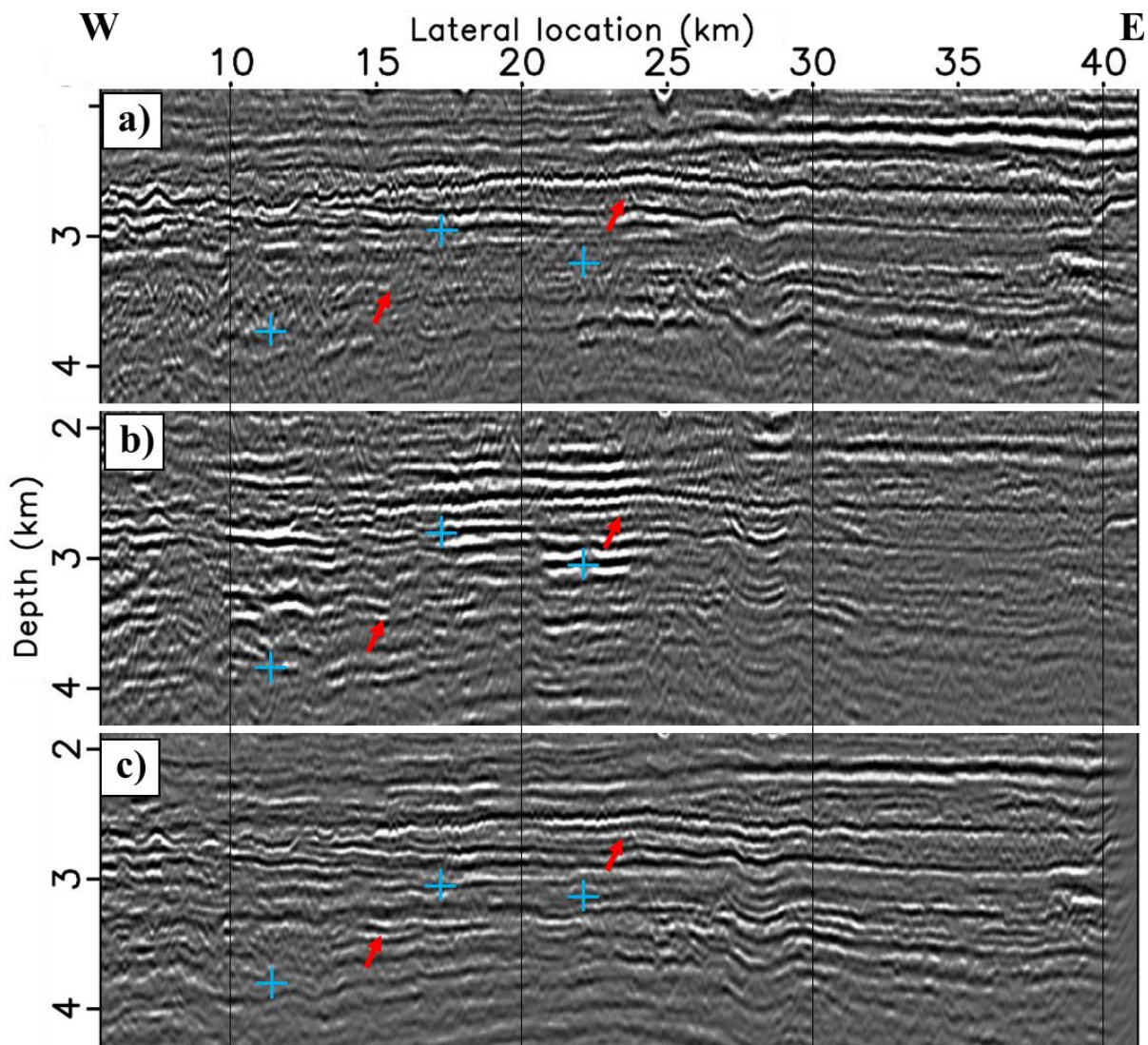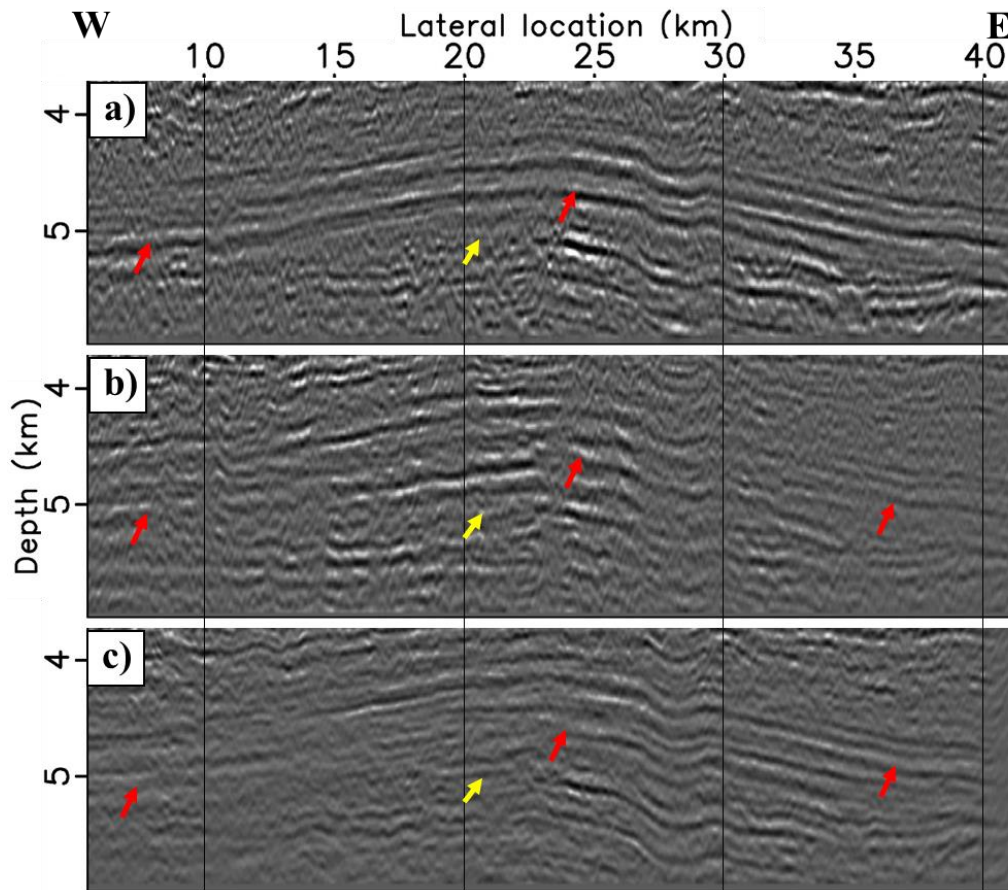

Figure 4.14: *Comparison of LSRTM primary image (a), LSMRTM surface multiple image and (c) FWM total image. The images are zoomed in between 4 - 6 km depths.*

5.   Field data application

Next, we demonstrate the application of the proposed methodology to a 2D field seismic data provided by Wintershall Dea Norge.

The main seismic parameters are defined in Table 5.1. The receiver depth had a slant geometry changing from 8 - 18 m (i.e. broadband acquisition geometry).

Table 5.1: *Data specifications*

Source interval, m	12.5
Source depth, m	6
Streamer length, m	6000
Receiver interval, m	12.5
Receiver depth, m	8 - 18
Channels per streamer	480
Number of shot gathers	1706
Max offset, m	6087
Min offset, m	94.5
Fold	240

5.1.   Velocity model building

Figure 5.1 demonstrates the velocity improvement going from a smooth initial model to a high-resolution velocity model obtained after FWI. A velocity model obtained from conventional velocity spectrum analysis was used as an initial starting point (Yilmaz, 2001). Figure 5.1a shows the starting initial model where one can see the strong velocity contrast at the sea bottom, velocity changes from 1450 m/s to 1600 m/s. From the sea bed velocity increases gradually up to around 4400 m/s in the deepest part of the model (Figure 5.1a). Velocity model and update after FATT is shown in Figure 5.1b and Figure 5.2a, respectively. Tomography mainly increased the velocities especially at the shallow part of the model by 80 - 400 m/s (Figure 5.2a). There is a notable decrease in the left side of the model where tomography in some locations decreased velocities up to 160 m/s. Some small structural (geological) details start to appear in the updated velocity model (Figure 5.1b)
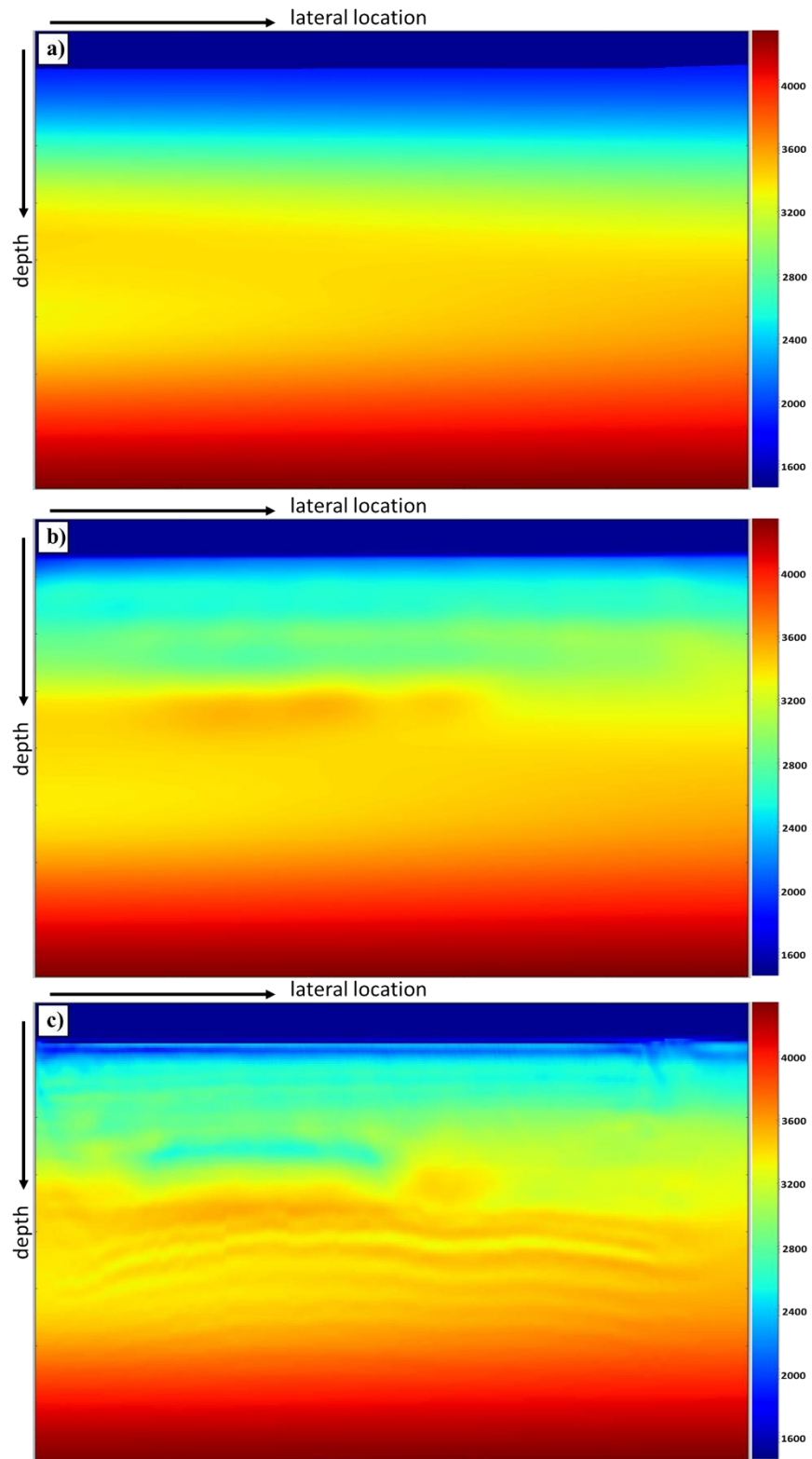
Figure 5.1: *Comparison of (a) initial, (b) after tomography and (c) after FWI velocity models.*

Note that FATT updated velocities only up to a certain depth level. As this is a technique based on using the refracted waves and is able recover mostly the near-surface, given the maximum offset is adequate (Jones, 2010).

Figure 5.1c shows the FWI result. The updates provided by FWI are clearly visible. Some geological trends are more recognizable. The shallow part of the model has a very smooth velocity structure, and reflectors have generally a flat geometry. This can also be seen in the velocity updates (Figure 5.2b), where velocity changes have flat and layering characteristics. In the deeper part (Figure 5.1c) the geological structures are recognizable. We can see the geometry of some layers. Reflector geometry is associated with fault blocks, and the discontinuity of reflectors match typical fault plane structures. There is a well-defined low-velocity anomaly captured on the left side of the model.
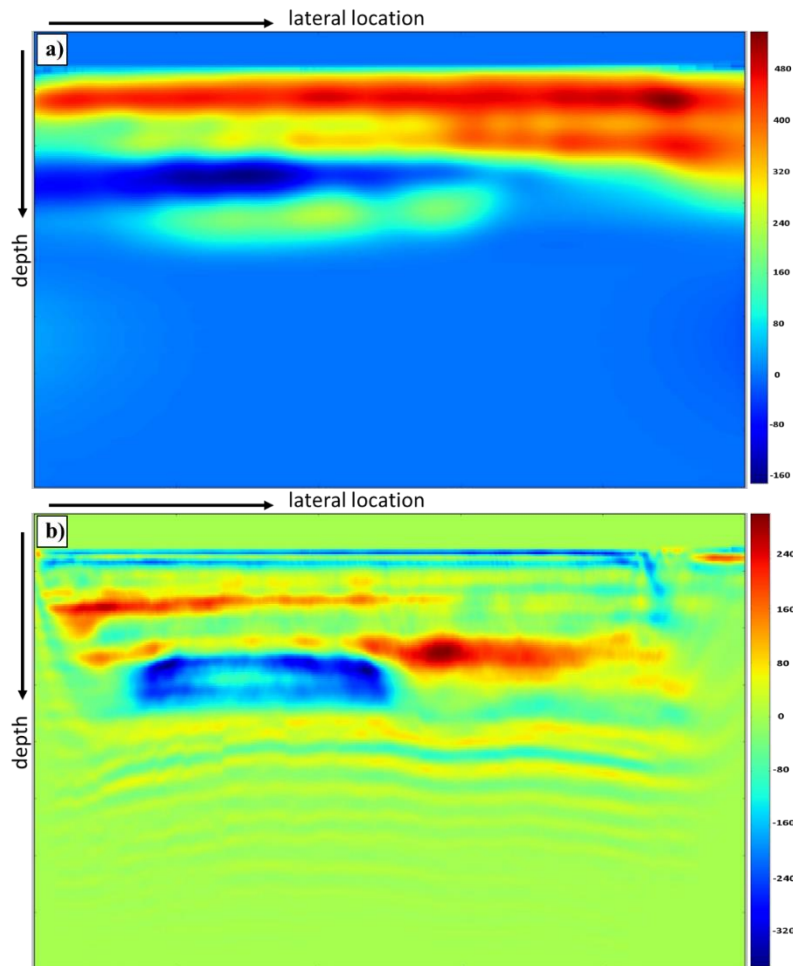
Figure 5.2: Velocity updates (a) after tomography and (b) after FWI.

To define the quality of the velocity model obtained by FWI we compared modeled data and observed data with initial and FWI updated models. Figure 5.3 shows the comparison plot. Comparison between the real shot gather and modelled shot gather derived from the initial velocity model show a clear mismatch between refraction events (Figure 5.3a). Using these velocities would certainly lead to cycle skipping problems in FWI where the inversion converges towards a local minima (Virieux and Operto, 2009). To avoid cycle skipping, FATT was used to ensure that the refractions events are within one half-cycle, before the application of FWI. Figure 5.3b demonstrates the comparison between the same real shot gather and a shot gather modeled using the updated velocities after FWI. We can observe a satisfactory match between the modelled and observed data. Refracted waves have identical phase and traveltimes. It means that the updated velocities accurately describe the wave kinematics from the subsurface geology. It also reduces the uncertainty of the depthing main events.
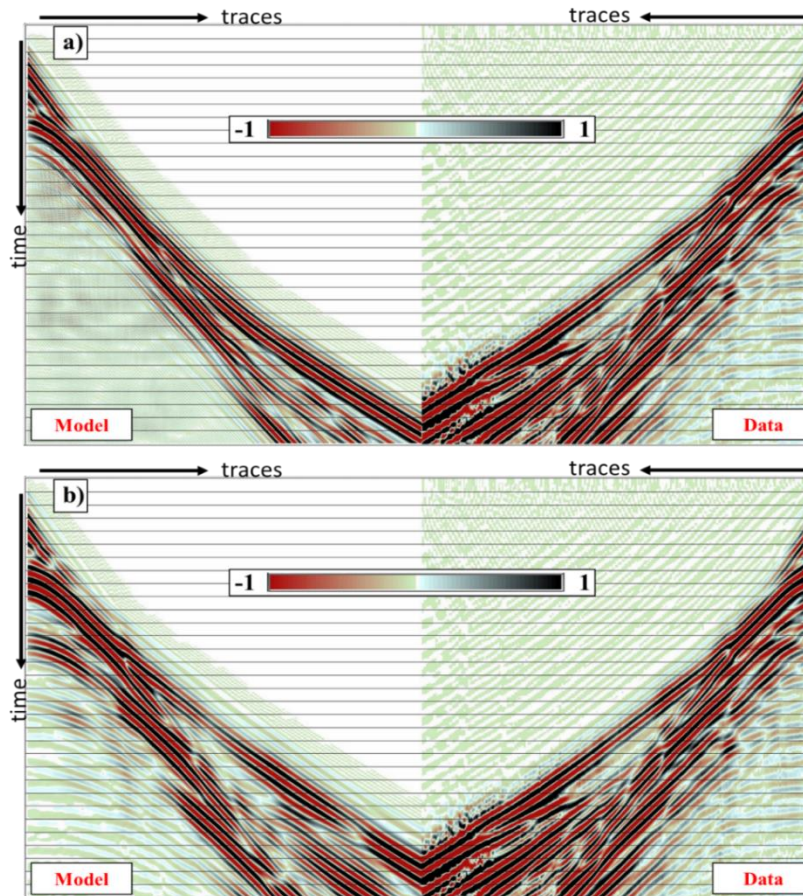
Figure 5.3: *Comparison of modelled and observed data with starting initial velocity model (Fig. 5.1a) (a) and FWI updated models (Fig. 5.1c) (b).*

5.2.   Preprocessing for imaging

Figure 5.4 shows an example of the provided data which consist of raw and deghosted shot gathers. The result of deghosting are demonstrated on the right side (Figure 5.4b). The preprocessing sequence applied to create deghosted gathers includes: removing the bubble effect of airguns and zero-phasing (i.e. designature), eliminating direct waves and removing ghost effect.
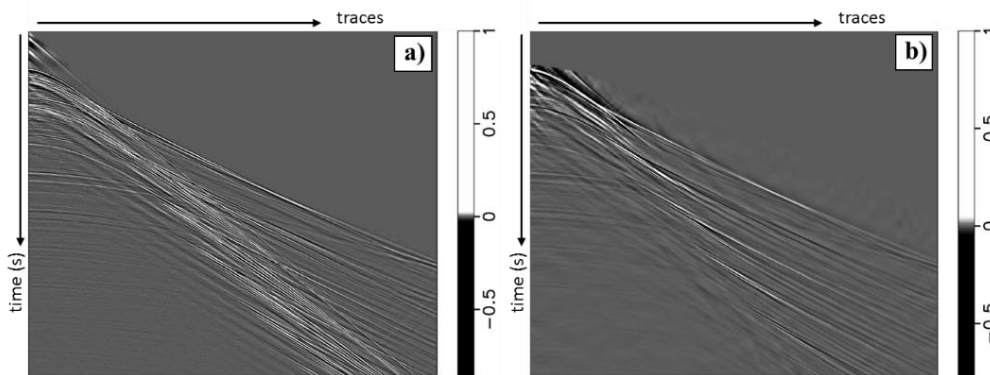
Figure 5.4: Raw (a) and deghosted (b) shot gather.

The visualization of the common offset (1000 m) gather provides a good insight into geological settings and identification of multiples (Figure 5.5a). The surface-related multiples generated from the sea bed are clearly visible as horizontal reflectors repeating the flat topography of the sea bed (indicated by red arrows), we are able to see second and third-order of multiples (Figure 5.5a). It means that, the velocity contrast is high at the seabed. Surface multiples of two strong reflectors (indicated by the yellow and green arrows) are well observed. The configuration of the deeper reflectors, which is marked by the green arrows, shows a slight dipping trend while all reflectors above it have a relatively flat configuration.

Figure 5.5b shows split primaries from multiples. We can see that SRME has modeled and adaptively subtracted most of the multiples. Comparing with data before SRME (Figure 5.5a) there are no more repeating reflectors observed proving the effectiveness of SRME. However, some weak amplitude residuals of multiples can be seen. These residuals have high-frequency characteristic meaning that SRME was able to resolve the low-frequency component of multiples. Even though the SRME methods did not work perfectly, in this study, we consider this SRME output is suitable for imaging. There is no doubt that a more suited processing sequence can abd should be applied to reduce the amount of residual multiple energy still present in the data (Dragoset et al., 2010).
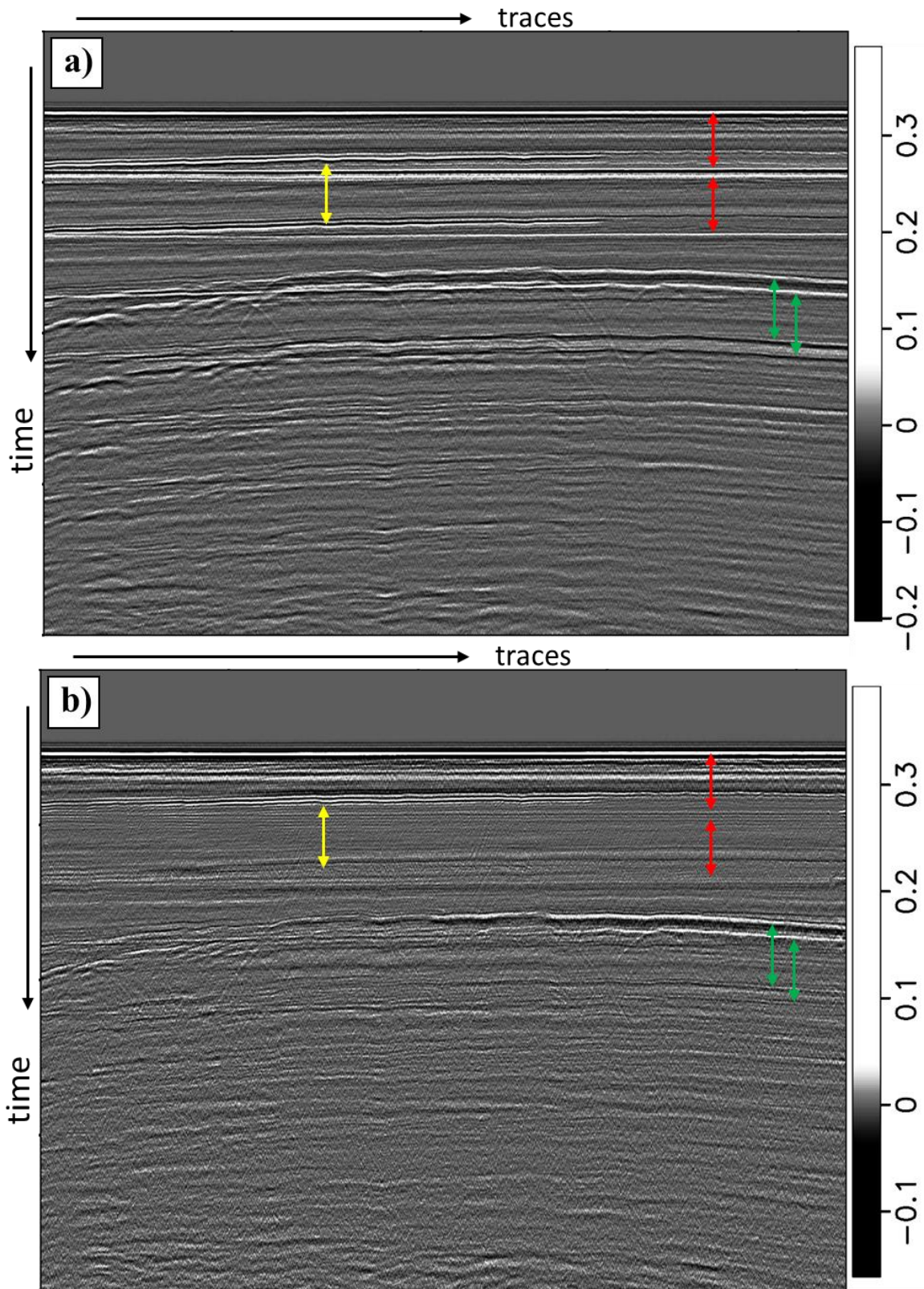
Figure 5.5: *Common offset gather showing data before (a) and after SRME.*

5.3. Imaging

Next, we demonstrate the results of the application of the proposed methodology on the 2D broadband data.

The shot gathers used during the imaging processes are shown in Figure 5.6.We can see that multiple shot gather have predominantly low-frequencies compared with the primaries. Before implementing FWM method, total data (Figure 5.6a) was muted (indicated by the red dashed line) to remove refraction events.
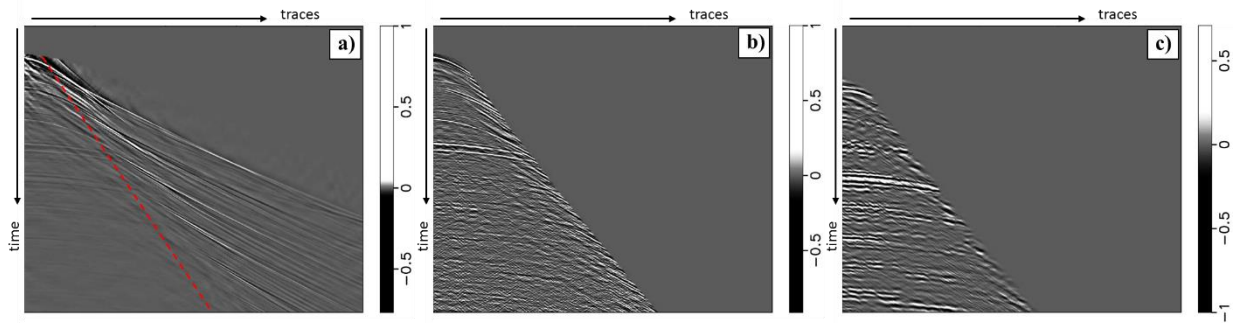
Figure 5.6: Total data (a), primaries (b) and surface multiples (c).

Figure 5.7 shows the final results of imaging with the primary reflections. Due to computational time limits and fewer benefits coming from more iteration of least-squares approach the final LSRTM image was obtained after the iteration7 and LSMRTM after the iteration 4. Amplitude scales averaged globally (-1 to 1) for vizualization conviennience.

It is notable that LSRTM produced a sharp image with very clear reflector pattern. The primary image has high resolution, reflectors are identifiable down to the area with fault blocks highlighted by dashed red rectangle. The shallow part of the image is horizontally layered, lateral continuity of reflectors is well observed. There is a low-frequency noise recognizable below the sea bed (Figure 5.7). Conventional RTM suffers from such low-frequency artifacts due to the presence of strong impedance contrast below the sea bed (Leveille et al., 2011). By applying LSRTM rather than RTM we reduced this noise effect. However, this low-frequency noise can be further attenuated by post-stack processing (Yilmaz, 2001). We can observe some small details around the sea bed (Figure 5.7, marked by green arrows) which indicates a signal-to-noise ratio of the obtained image. Ability to differentiate such shallow reflectors is not typical for most marine data, especially 3D and ocean bottom seismic (OBS) (Ikelle and Amundsen, 2005). Because of poor

source and receiver sampling, the shallow image will be less illuminated. In the present, the 2D data has 12.5 m source and receiver intervals which allowed us to get sufficient sampling to obtain a good image of shallow depths.
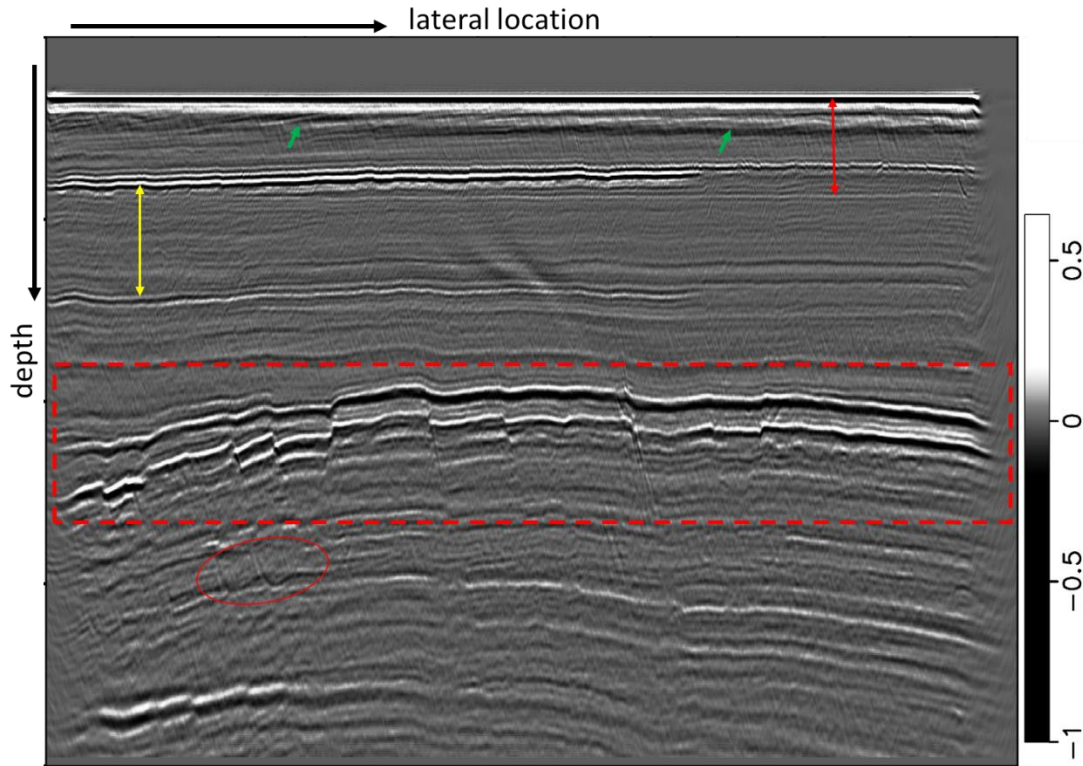
Figure 5.7: LSRTM imaging with primaries.

There is a flat and well recognizable reflector at the shallow part and its surface-related multiple artifact linked by yellow arrow (Figure 5.7). This reflector is a strong multiple generator, which causes artifacts in the primary image. This artifact can explained as a first-order surface-related multiple, i.e. reflection wave emitted from source bounces at this high contrast layer, travels back towards receivers, and then again bounces from free surface to the sea bed and finally recorded by receivers. Note that, this artifact is characterized by high frequencies. Indeed, the low-frequency component was effectively removed by the SRME. We can also distinguish a relatively weak sea bed first-order surface-related multiple artifact (Figure 5.7, indicated by the red arrow). SRME fails to adequately separate these multiple reflections, due to inaccurate prediction and adaptive subtraction (Dragoset et al., 2010).

The most prominent features in the primary image are the faulted reflectors in the depth part which are highlighted by the dashed red rectangle, where both reflectors and faults are clearly imaged

(Figure 5.7). The discontinuities related to faulting are easily identifiable. The high-quality illumination at this depth interval will enable us to conduct more accurate and consistent seismic interpretation at a later stage.

It is noticeable that in the deeper section (Figure 5.7) there are some 'smiling' events circled in red. The presence of such events indicates undermigration, because of low velocities in that depth interval (Yilmaz, 2001). As mentioned in section 4.4, in order to improve imaging of deeper section, the velocity model building workflow can be extended by combining FWI with migration velocity analysis or reflection tomography (Jones, 2010).

Figure 5.8 shows the result of LSMRTM imaging at the 4th iteration. We can divide the multiple image section into four zones (Figure 5.8). The first-order surface-related multiple image at the shallow depth (zone I) has a quite good illumination. We can identify small features below the sea bed marked by green arrows. Furthermore, the strong reflector (indicated by the red arrows) is clearly imaged and its continuous geometry is well observed.

As we can observe, the first-order surface multiple image is contaminated with artifacts. In the depth level of zone II primary residuals (Figure 5.8, indicated by the yellow arrows) are imaged. As we discussed earlier, LSMRTM, the methodology of imaging the first-order surface-related multiples, requires the primaries as a source side wavefield and the first-order surface-related multiples as a receiver side wavefield. However, using SRME as the only demultiple technique leads to an imperfect primary dataset and the subtracted multiples consist of all orders of surface related multiples. The perfect prediction of multiples by SRME can be obtained under several assumptions (Dragoset et al., 2010): source wavelet estimated correctly, wide-azimuth 3D acquisition geometry and perfect adaptive subtraction. In practice, because of 2D assumption, and changes in amplitude and phase of the source wavelet due to propagation in the subsurface the output of SRME gives poor results. It is possible to improve the separation of surface-related multiples and primaries by implementing iterative adaptive subtraction (Dragoset et al., 2010) and combining SRME with other demultiple algorithms (Weglein et al., 2011). However, detailed discussion and application of different multiple elimination technique are beyond the scope of this study.

In the deeper part of the first-order surface-related multiple image (zone III), the illumination of faulted reflectors is poor: The reflectors are less coherent with weak amplitudes (Figure 5.8, indicated by the red arrows). Even though there are no conflicting artifacts, due to weak surface-related multiple energy coming in from this depth interval, the reflectors are difficult to differentiate and we can observe the lack of high-resolution features.

It is noticeable that in the zone IV (Figure 5.8) no significant reflectors can be identified, events are distorted and pattern of reflectors correlates with faulted reflectors from the zone III. We explained these artifacts as higher-order surface multiples from the reflectors from the zone III.
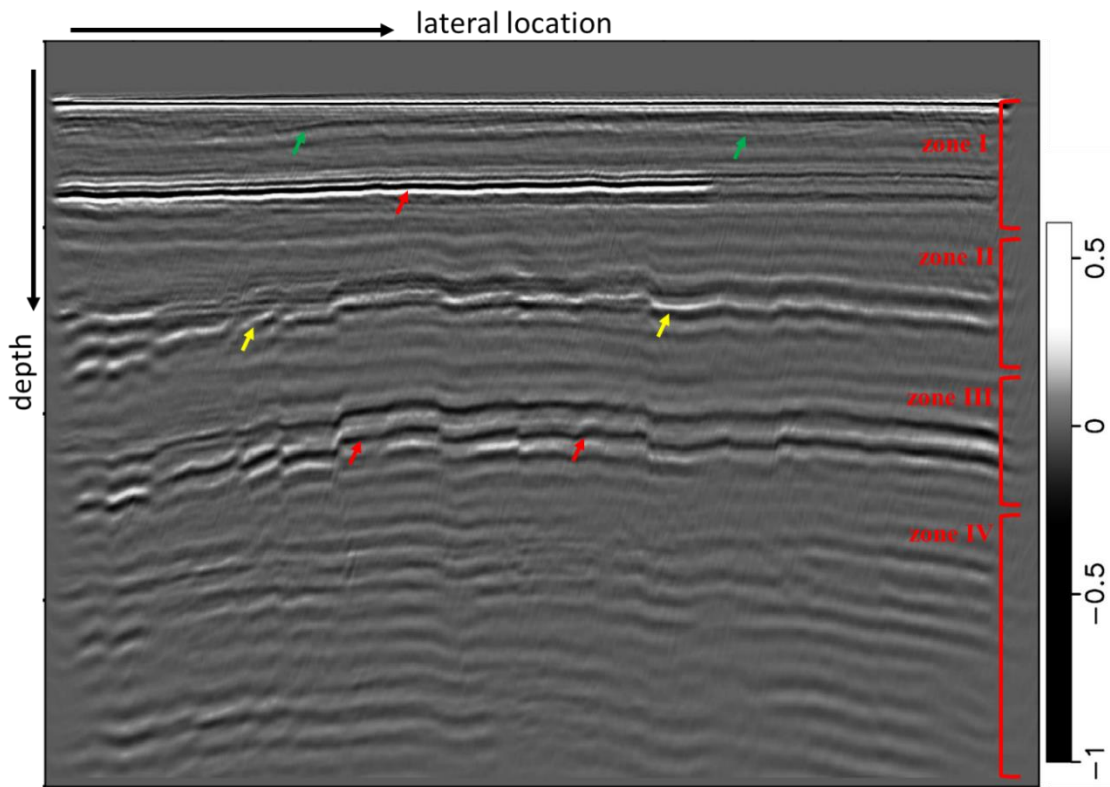
Figure 5.8: LSMRTM imaging with first order surface multiples.

The results of FWM imaging with total reflection data at the 9th iteration are illustrated in Figure 5.9a. The FWM image is truncated after the depth interval just below the faulted reflectors. Comparing with LSRTM (Figure 5.7) and LSMRTM (Figure 5.8) images, the subsurface image in the FWM method is not well reconstructed (Figure 5.9a). Even though the migrated image is in the true depth, the illumination of the FWM total reflection image is poor, and multiple artifacts are not resolved properly. In Figure 5.9a the residual artifact and reflectors from which they are

originated are linked by arrows. As we can observe, these residuals relate to first-order surface-related multiples.

The faulted structure indicated by red dashed rectangle (Figure 5.9a) has poor resolution, and reflectors and fault planes in this interval cannot be confidently interpreted.

It is visible that the illumination in the FWM total reflection image (Figure 5.9a) is not comparable with the LSRTM primary image (Figure 5.7) as it was for the Chevron synthetic data. As we mentioned in section 2.4, FWM based on estimating the reflectivity while minimizing the difference between modeled and observed data, and FWMod produces the synthetic data based on 2D assumption of the subsurface (Davydenko, 2016). Our results with FWM demonstrate that, when we are using the 2D FWM algorithms with multiple reflection rich data, the algorithm cannot properly accommodate the 3D complexity of subsurface geology. Because the field data represents 3D subsurface, even though it is acquired as a 2D data.

When waves are emitted from a seismic source and then are recorded by receivers, the amplitudes of the waves, during subsurface propagation, are affected by the divergence of the wavefront and absorption (Sheriff and Geldart, 1995). In primary imaging, amplitude corrections (i.e. geometrical spreading, attenuation, time-variant gaining) are applied to compensate the amplitude decay (Yilmaz, 2001). However, due complex ray paths of multiple events, it is very difficult to define the correct amplitude compensation for multiples. To illustrate the effect of amplitude compensation for multiples we applied constant gaining function with power 0.5 and 2 (Figure 5.9b and c). As we can see, the FWM algorithm depending on the gaining value produces different images. The FWM image with gaining function with power of 2 shows that the strong multiple artifact (Figure 5.9c, marked by the red arrows) is almost resolved, since the artifact is not clearly observed. Figure 5.9b shows the total reflection image after applying gaining function with power 0.5, the strong artifact is presented and its continuity well observed. Note also that, the depth interval circled in red is better illuminated in the case of gaining with power 2 (Figure 5.9c) However, the artifact from the seabed becomes stronger when gaining with power 2, while in the image with less gaining this artifact is less observable.

The obtained results of implementing FWM with 2D assumption on 3D data (i.e. the 2D field data actually represent the 3D earth) illustrated that the contribution from surface-related and interval

multiples cannot be clearly identified and the illumination is not comparable with the LSRTM primary image. To the overcome these FWM limitations and achieve a proper imaging of the surface-related and internal multiples on field seismic data, instead of using FWM with 2D assumptions it is possible to use 3D FWM. The 3D FWM algorithm accommodates a 3D earth more properly, and the amplitudes of waves can be handled more accurately (Davydenko, 2016).

Due time limitation of the thesis and the high computational cost of 3D processing, we could not afford the application of FWM on 3D seismic filed data in this study.

The application of out methodology on 2D field data can be summarized as follows:

1) LSRTM imaging with primaries produces the high-resolution subsurface image, where the faulted structure are clearly focused. However, there are some residual crosstalk from the surface-related multiples presented in the image due to imperfect multiples separation;

2) LSMRTM imaging provides a good illumination, and it is capable to reconstruct small-scale structures at the shallow depth. The contribution coming from first-order surface-related multiples is comparable with primaries at the shallow depths. However, the deeper part of LSMRTM image contaminated with artifacts due to imperfect primary and multiple separation by SRME. To remove artifacts from higher order surface-related multiples, SRME algorithm can be extended in such a way that it produces first-order surface-related multiples only;

3) Without taking into account properly the amplitudes of reflection events (both primaries and multiples), FWM imaging with total reflection data cannot accurately accommodate multiple reflection energy. To overcome this problem we should use 3D FWM on 3D acquired data.
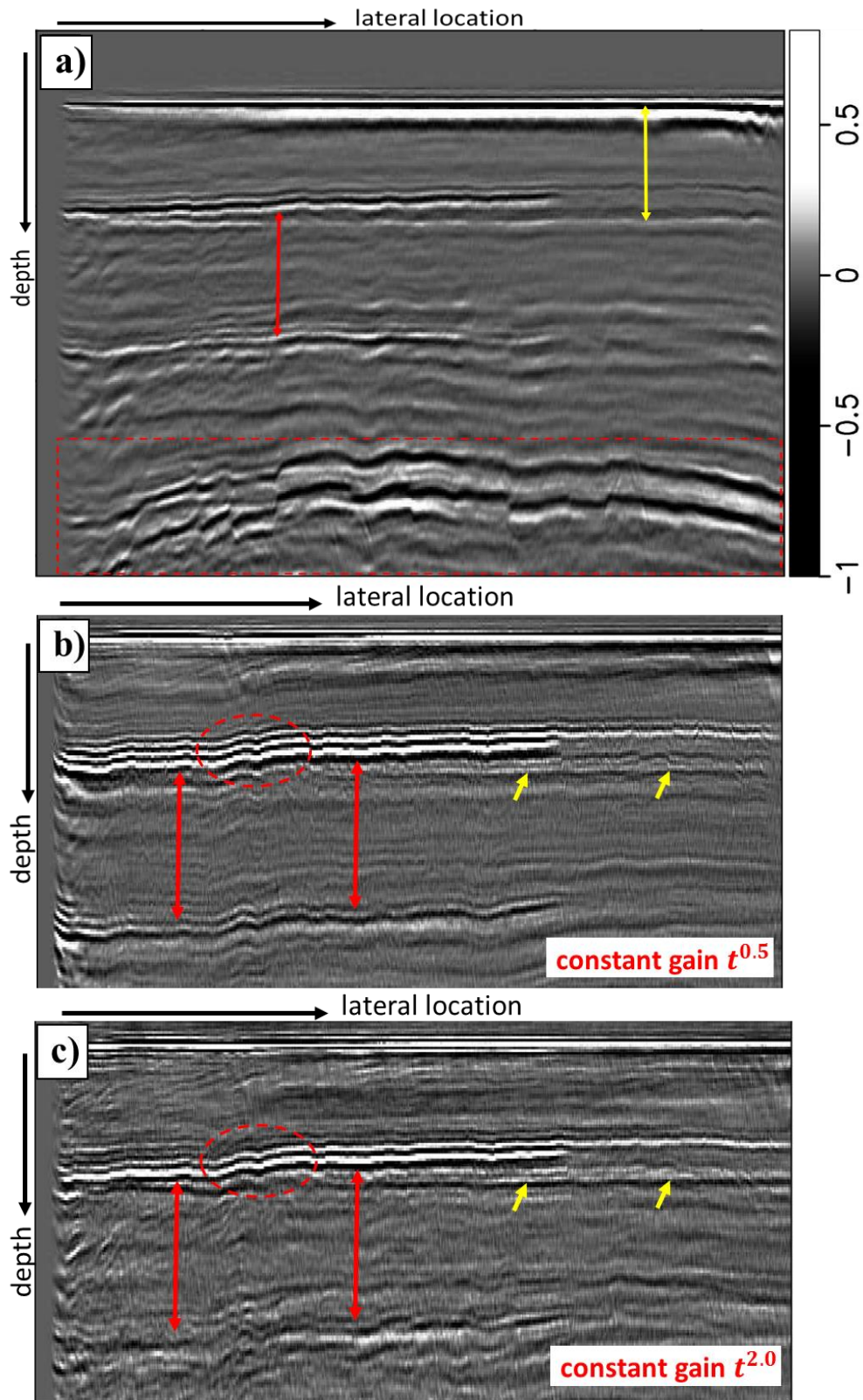
Figure 5.9: *(a) FWM imaging with total reflection data. (b) and (c) Enlargement of a portion (a), showing illumination changes due different gaining.*

6. Discussion and conclusions

In this thesis, we reviewed the advantages related to using multiples in imaging, and introduced a robust workflow for depth migration and velocity model building to obtain an accurate and detailed subsurface image. The workflow consists of two main parts: velocity model building and imaging with different reflection events. The aim of this study was to take a step toward incorporating the information from surface-related and internal multiples for subsurface illumination, and to better understand imaging challenges and limitations when imaging with multiples.

The workflow was tested on the Chevron 2D marine synthetic and on a 2D broadband field seismic datasets. Firstly, we successfully implemented FATT, which mainly updated velocities at shallow depths, to obtain a good initial velocity model. Second, we applied FWI to produce a high-resolution velocity model for depth migration. Then, we used LSRTM, LSMRTM and FWM to image primaries, surface-related multiples and total reflections (i.e. primaries, surface-related and interval multiples together). Finally, we determined the contribution from different reflection events to illuminate the subsurface.

Furthermore, we discussed the main findings and contributions in this study, and proposed recommendations for future work.

6.1. Velocity model building

Velocity model building for the synthetic and field datasets showed that combination of FATT and FWI produced an accurate, high-resolution velocity model up to a certain depth. The output of FATT provides a good initial model for FWI, which helped resolve cycle skipping, and ensured the algorithm did not get trapped in a poor local minimum.

The mentioned approach for velocity model building makes depth imaging more robust and practical, and enables us to avoid the depth-time conversion uncertainty related to conventional imaging in the time domain (Herron, 2011). We demonstrated that the output of FWI resembles a migrated image, with the prevailed influence of the low-frequency wavefield. It can be used to quality control the subsurface image. The FWI velocities can be used as a link between processing and interpretation, as some low-velocity anomalies are easier to visualize in the velocity model than the final image. It is seen in the field data example, where a low-velocity anomaly was

captured in the velocity model obtained from FWI, but the reflector geometry is not affected by this anomaly.

Appendix A contains the comparison of the velocity model obtained by our approach, and the one obtained by conventional velocity picking, for the field dataset. The improvement and additional information about the subsurface geometry obtained by using FWI is clearly observed.

In order to update the deeper part of the velocity model, we can suggest to extend the workflow by including the reflection traveltime tomography and migration velocity analysis (Jones, 2010).

6.2. Imaging with primaries

The primary images obtained by LSRTM produces a well illuminated, and sharp subsurface image. There is poor continuity at shallow depths for the synthetic data example. Furthermore, some reflectors are distorted due to the imperfect primary and multiple separations in depth intervals where the velocity has noticeable decreases. The illumination of the synthetic image at the deeper part shows continuous reflectors.

As earlier discussed (section 1.4) Davydenko and Verschuur (2017) showed that when multiples are treated as noise, iterative elimination of multiples by conventional seismic processing does not always guarantee the perfect result. In complex geological settings, multiples can be superimposed with primaries in a way that their poor separation can lead to distortions in the primary image. In conventional Kirchhoff pre-stack time migration (Appendix A, Figure A.2a) primaries are distorted at certain depths due to strong demultiple which leads to an accurate seismic interpretation. However, in the same interval, the LSRTM image enable us to distinguish reflector geometry. Consequently, treating multiples as noise, and only imaging primaries works for identifying and mapping of the specific targets. When multiples are properly taken into account, they allow us to produce a subsurface image with a broader application, such as a better understanding of the basin evolution as a whole, rather than just specific intervals.

The major advantages of LSRTM imaging with primaries are clearly visible when imaging the prominent structural features of the field data. The fault planes and reflectors around the faulted interval have higher resolution, resulting in proper imaging of the fault block, compared to conventional Kirchhoff migration (Appendix A, Figure A.2).

6.3.   Imaging with surface-related multiples

LSMRTM imaging with first-order surface multiples is capable of providing an accurate and well-illuminated image for the shallow depths. This is a major advantage of including surface-related multiples into the imaging process. Improved shallow images can be used to image below shallow targets and allow the identification of drilling hazards related to overpressure zones (Ikelle and Amundsen, 2005).

The results of LSMRTM imaging with synthetic and field datasets illustrated the comparability of shallow depth illumination of the surface-related multiple image with the primary image. The added value of first-order surface-related multiples is clearly observable at the shallow depth, the continuity of reflector geometry is captured quite well, we are able to distinguish finer details of the subsurface geology. When the steep-dip events are present at shallow depth, the information coming from surface-related multiples due to more narrow-angle coverage, leads to poor illumination of these events. Consequently, the primary and the surface-related multiple reflections should be incorporated to get an improved image of steep-dip events.

The deeper part of surface-related multiple image is poorly illuminated, and the information coming from the surface-related multiples cannot replace the primary reflection contribution.

In LSMRTM, the methodology for migrating the surface-related multiples requires using the primaries as a source and first-order multiples as the data. The output of SRME contains first-order as well as all higher orders surface-related multiples. In this work, we considered the output of SRME suitable for LSMRTM imaging and expected that the artifacts coming from higher orders multiples would be insignificant. However, the results of LSMRTM imaging with the synthetic and field data demonstrated the presence of relatively strong artifacts from higher orders multiples. These artifacts distort the LSMRTM image in the same way as multiples distort the conventional primary image. To overcome this limitation we suggest to extend SRME algorithms to predict and then subtract only first-order surface multiples. That might reduce the artifact effects of the deeper part of the LSMRTM image.

6.4.   Imaging with total reflection data

FWM imaging with total reflection data shows much promise to incorporate the surface-related and internal multiples together rather than imaging multiples by separating them from primaries. The FWM with synthetic data produced much cleaner, more interpretable, and good illumination at each depth interval. The total reflection image has improved in terms of the amplitude distribution, the continuity of reflectors is clearly visible from the shallow to deeper depths. Comparing with LSRTM and LSMRTM images, FWM produces an artifact-free subsurface image. This advantage of FWM algorithm is clearly observable at the shallow depths in the image of the Chevron data.

However, the deepest reflectors have less continuity geometry in FWM image, while the same reflectors are better focused, and more interpretable in the LSRTM primary image. We explained this limitation of FWM by its sensitivity to the accuracy of the velocity model. When velocities are poorly defined (in our case for depths below 4 km), this method cannot properly focus some reflectors.

The added value coming from the internal multiples can be observed when implementing FWM on the synthetic data. In the depth interval with notable decrease of velocity, we determined that LSRTM and LSMRTM images are distorted and contaminated by crosstalks. On the other hand, the FWM image provides an enhanced image enabling us to distinguish the finer details in the image.

The obtained results of implementing FWM on the 2D field data illustrated that the contribution from surface-related and interval multiples cannot be clearly identified. The illumination of FWM is poor and is not comparable with the LSRTM primary image. To overcome this limitation, we suggest that instead of using FWM with 2D assumptions we should use the 3D FWM. The 3D FWM algorithm accommodates a 3D earth more properly, allowing the amplitudes of waves to be handled more accurately (Davydenko, 2016).

Appendix A

In this section, we present the comparison of primary images produced by our methodology and conventional Kirchhoff time pre-stack migration. The result of Kirchhoff migration is provided by Wintershall Dea Norge.

Figure A.1 shows the comparison of primary images produced by applying Kirchhoff time migration. The conventional time image obtained after processing sequence, which mainly includes: noise attenuation (i.e. swell, direct, linear), deghosting, iterative multiple elimination (SRME, Tau-P muting, Parabolic Radon demultiple), amplitude scaling and 2D Kirchhoff Pre-stack Time Migration (PreSTM). Note that, both in LSRTM and PreSTM imaging only primary reflection used and multiples removed prior imaging. Furthermore, LSRTM image converted from depth domain to time domain using the velocity model after FWI. Amplitude scales are relative, scaled globally from -1 to 1.

The PreSTM and LSRTM images shown in Figure A.1a and Figure A.1b, respectively. As we can see PreSTM image balanced better in terms of amplitude distribution. There is no low-frequency noise below the sea bed while in LSRTM we can observe this type of noise. The residual artifact from surface multiples is not observable in PreSTM image (Figure A.1a, indicated by the yellow arrows) while in LSRTM image this artifact presented. The deep part of sections illustrates almost same structure with almost no observable reflectors.

It is noticeable that the faulted area (indicated by black arrows) in LSRTM (Figure A.1b) imaged better and events have more coherent characteristics, we can see more clearly the fault planes, and sharp reflector terminations are more interpretable.

Figure A.2 demonstrates zoomed interval of the main structural features in the field data which consist of strong amplitude faulted reflectors. We can describe this zoomed section dividing it into two zones (Figure A.2). As we can see, reflections from fault planes are imaged clearly in LSRTM imaging. However, due to more enhanced processing some reflectors have better lateral continuity in PreSTM image (Figure A.2a). Zone II has better signal-to-noise ratio, reflectors identification and their distinctive patterns well observed while in zone I seismic facies cannot be easily mapped because poor signal-to-noise ratio, i.e. weak reflections.

It is noticeable that the LSRTM image in zone I contains surface multiple artifacts (Figure 5.12b, indicated by yellow arrows). As we described earlier, these residuals multiple energy due to imperfect primary and multiple separation in our methodology. Note also that these, artifacts mostly characterized by high frequencies.

As we can observe, multiple artifacts presented in the LSRTM image are eliminated in the PreSTM image (Figure A.2b, indicated by the yellow arrows). As we mentioned earlier in this section, in the PreSTM imaging approach, multiple waves were eliminated iteratively by combining several demultiple algorithms. However, due to close velocity behavior of multiples and primaries, and complex multiple reverberations, in PreSTM processing primaries are distorted because of fail of demultiple algorithms. That means that in complex geological and acquisition settings we could have a situation when primary image will be distorted while trying to separate multiples.

There are no detectible reflectors in the PreSTM image in zone I (Figure A.2a). We cannot distinguish reflectors continuity and define clearly any seismic facies within this part of section in PreSTM image. On the other hand, application of our imaging approach with less aggressive demultiple separation demonstrates the ability to interpret reflectors in this interval. For example, the reflectors indicated by black arrows in Figure A.2 are imaged better in LSRTM method and distorted in PreSTM imaging. Basically, in the PreSTM imaging, which can be referred as the target oriented approach, an uninteresting area is sacrificed (zone I) and imaging focused in the faulted reflectors (zone II). That means that the PreSTM image useful for identifying and subsurface mapping of exploration targets, while the LSRTM image has broader application, such as better understanding the basin evolution as a whole rather than just specific intervals.
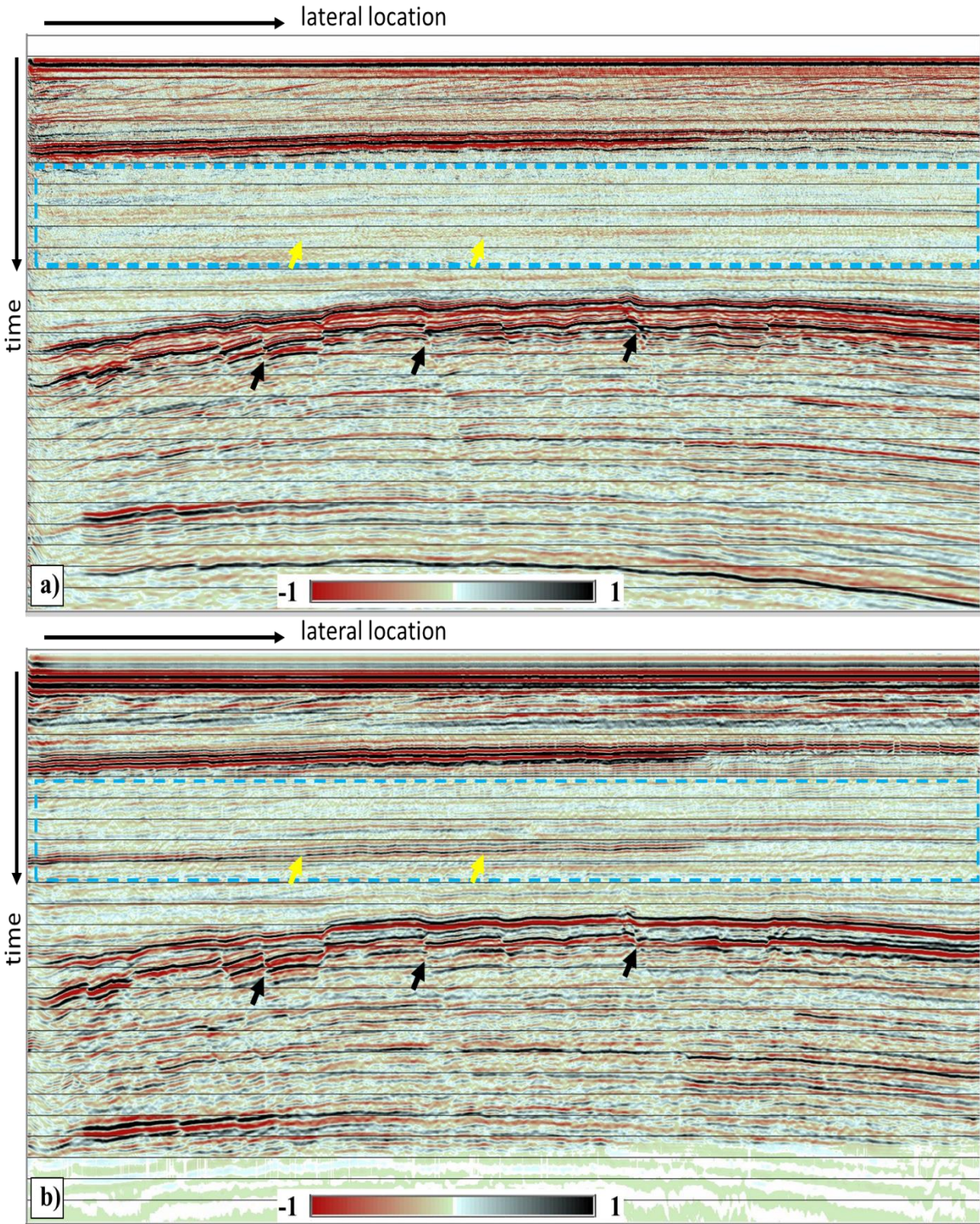
***Figure A.1****: Primary imaging with PreSTM (a) and LSRTM (b).*
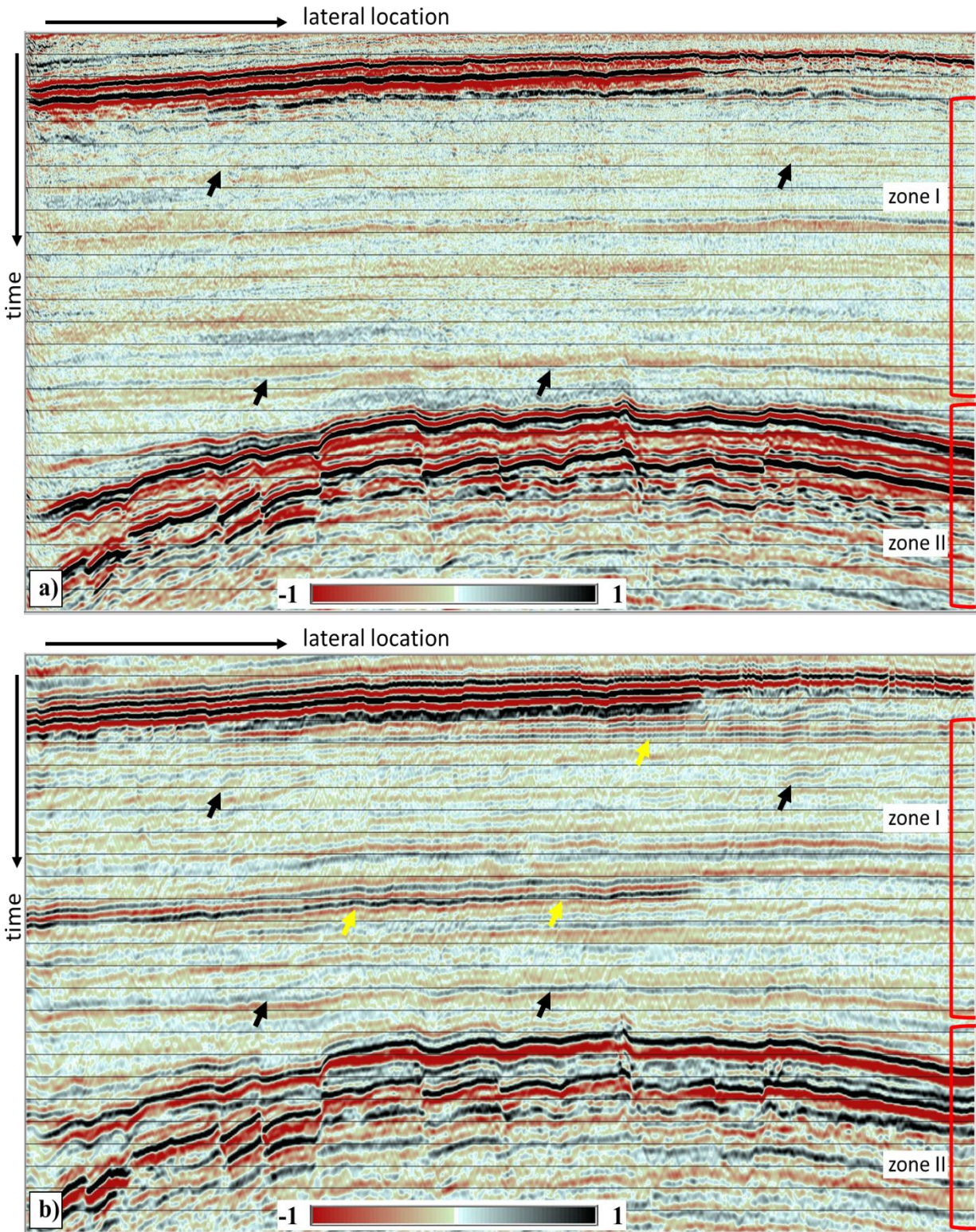
Figure A.2: *Primary imaging with PreSTM (a) and LSRTM (b). The images are zoomed at time interval to facilitate most prominent features.*

In Figure A.3 shown the comparison of the velocity models obtained by combination of FATT and FWI methods, and the conventional picked velocity model. Note that, the velocity model used for PreSTM imaging (Figure A.3a) converted from root-mean-square velocity (V_{RMS}) to interval velocity in depth.

Figure A.3b demonstrates much more details of velocity structures while V_{RMS} picked model (Figure A.3a) shows a major regional trends within data. The low-velocity anomaly zone circled in yellow clearly captured in velocity model after FWI. Furthermore, the improvement in the deeper part of the model clearly seen in velocity model obtained by our methodology, reflectors configuration can be recognized (Figure A.3b, indicated by the black arrows).

Note also that, V_{RMS} picked model describes mostly macro features and there is no identifiable correlation between the image (Figure A.1a) and velocity model (Figure A.3a). However, there is a clear correlation between LSRTM image (Figure A.1b) and velocity model after FWI (Figure A.1b and Figure 5.1c), we can observe that velocity model proportional to subsurface image with prevailed influence of low-frequency wavefield. This means that, using information coming from FWI velocity model we are able to reduce the ambiguity in seismic interpretation, and to avoid the depth-time conversion uncertainty related to conventional imaging in time domain (Herron, 2011)
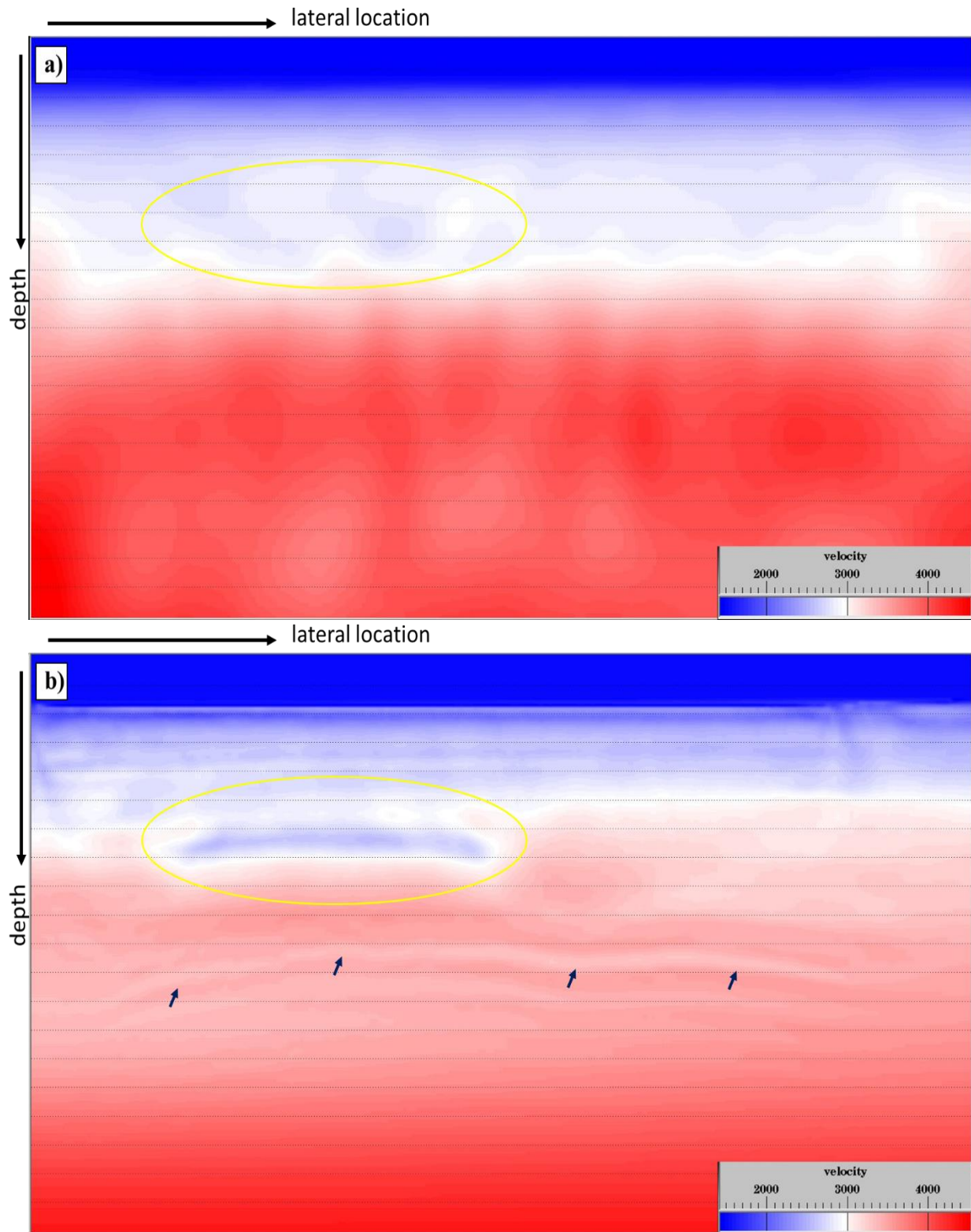
Figure A.3: After conventional velocity picking analysis (a) and interval velocities in depth obtained after FATT and FWI (b)

References

Baysal, E., D. Kosloff, and J. Sherwood, 1983, Reverse time migration: Geophysics, v. 48, p. 1514-1524.

Berkhout, A. J., 1982, Seismic migration, imaging of acoustic energy by wave field extrapolation: A: theoretical aspects, Elsevier.

Berkhout, A. J., 2014, Review Paper: An outlook on the future of seismic imaging, Part II: Full-Wavefield Migration: Geophysical Prospecting, v. 62, p. 931-949.

Berkhout, A. J., and D. J. Verschuur, 1994, Multiple technology: Part 2, Migration of multiple reflections, SEG Technical Program Expanded Abstracts p. 1497-1500.

Berkhout, A. J., and D. J. Verschuur, 2006, Imaging of multiple reflections: Geophysics, v. 71, p. SI209-SI220.

Choi, Y., and T. Alkhalifah, 2012, Application of multi-source waveform inversion to marine streamer data using the global correlation norm: Geophysical Prospecting, v. 60, p. 748-758.

Claerbout, J. F., 1985, Imaging the earth's interior, Blackwell Scientific Publications.

Davydenko, M., 2016, Full wavefield migration: Seismic imaging using multiple scattering effects: PhD thesis, Delft University of Technology.

Davydenko, M., and D. J. Verschuur, 2017, Full-wavefield migration: using surface and internal multiples in imaging: Geophysical Prospecting, v. 65, p. 7-21.

Dragoset, B., 1999, A practical approach to surface multiple attenuation: The Leading Edge, v. 18, p. 104–108.

Dragoset, B., E. Verschuur, M. I., and R. Bisley, 2010, A perspective on 3D surface-related multiple elimination: Geophysics, v. 75, p. 75A245-75A261.

Dragoset, W. H., and Ž. Jeričević, 1998, Some remarks on surface multiple attenuation: Geophysics, v. 63, p. 772-789.

Fichtner, A., 2011, Full Seismic Waveform Modelling and Inversion, Springer.

Guitton, A., 2002, Shot-profile migration of multiple reflections, SEG Technical Program Expanded Abstracts p. 1296–1299.

Herron, A. D., 2011, First Steps in Seismic Interpretation, Society of Exploration Geophysicists.

Ikelle, L., and L. Amundsen, 2005, Introduction to Petroleum Seismology: Tulsa, OK, Society of Exploration Geophysicists.

Jones, F. I., 2010, An Introduction To: Velocity Model Building, EAGE.

Lailly, P., 1983, The seismic inverse problem as a sequence of before stack migrations, Conference on Inverse Scattering, Theory and Application, Society for Industrial and Applied Mathematics, Expanded Abstracts, p. 206–220.

Leveille, P. J., F. I. Jones, Z. Zhou, B. Wang, and F. Liu, 2011, Subsalt imaging for exploration, production, and development: A review: Geophysics, v. 76, p. WB3-WB20.

Liner, L. C., 2016, Elements of 3D seismology: Tulsa, OK, Society of Exploration Geophysicists.

Liu, Y., X. Chang, D. Jin, R. He, H. Sun, and Y. Zheng, 2011, Reverse time migration of multiples for subsalt imaging: Geophysics, v. 76, p. WB209-WB216.

Lu, S., D. Whitmore, A. Valenciano, and N. Chemingui, 2014, Enhanced subsurface illumination from separated wavefield imaging: First Break, v. 32, p. 87–92.

Lu, S., D. N. Whitmore, A. A. Valenciano, and N. Chemingui, 2015, Separated-wavefield imaging using primary and multiple energy: The Leading Edge, v. 34, p. 770-778.

Malcolm, A. E., U. Bjørn, and M. V. de Hoop, 2009, Seismic imaging and illumination with internal multiples: Geophysical Journal International, v. 176, p. 847-864.

Nemeth, T., C. Wu, and G. Schuster, 1999, Least-squares migration of incomplete reflection data: Geophysics, v. 64, p. 208-221.

Schuster, G., 2009, Seismic Interferometry, Cambridge University Press.

Sheriff, R. E., and L. P. Geldart, 1995, Exploration Seismology: Cambridge, Cambridge University Press.

Sirgue, L., O. I. Barkved, J. P. Van Gestel, O. J. Askim, and K. J. H., 2009, 3D waveform inversion on Valhall wide-azimuth OBC, 71st Conference & Exhibition, EAGE, Extended Abstracts.

Sirgue, L., and R. G. Pratt, 2004, Efficient waveform inversion and imaging: A strategy for selecting temporal frequencies: Geophysics, v. 69, p. 231-248.

Taillandier, C., M. Noble, H. Chauris, and H. Calandra, 2009, First-arrival traveltime tomography based on the adjoint-state method: Geophysics, v. 74, p. WCB1-WCB10.

Tarantola, A., 1984, Inversion of seismic reflection data in the acoustic approximation: Geophysics, v. 49, p. 1259-1266.

Tarantola, A., 1987, Inverse Problem Theory: Methods For Data Fitting and Model Parameter Estimation, v. 130, Elsevier Science Publ. Co.

Verschuur, D. J., 1991, Surface-related multiple elimination, an inversion approach: Ph.D. dissertation thesis, Delft University ofTechnology.

Virieux, J., and S. Operto, 2009, An overview of full-waveform inversion in exploration geophysics: Geophysics, v. 74, p. WCC1-WCC26.

Weglein, A., S. Hsu, P. Terenghi, X. Li, and R. Stolt, 2011, Multiple attenuation: Recent advances and the road ahead The Leading Edge, v. 30, p. 864-875.

Weibull, W. W., and B. Arntsen, 2014, Reverse-time demigration using the extended-imaging condition: Geophysics, v. 79, p. WA97-WA105.

Whitmore, N. D., 1983, Iterative depth migration by backward time propagation, SEG Technical Program Expanded Abstracts 1983: SEG Technical Program Expanded Abstracts, Society of Exploration Geophysicists, p. 382-385.

Whitmore, N. D., A. A. Valenciano, W. Sollner, and S. Lu, 2010, Imaging of primaries and multiples using a dual-sensor towed streamer, SEG Technical Program Expanded Abstracts p. 3187-3192.

Wiggins, J., 1988, Attenuation of complex water-bottom multiples by wave-equation-based prediction and subtraction: Geophysics, v. 53, p. 1527-1539.

Yang, Z., J. Hembd, H. Chen, and J. Yang, 2015, Reverse time migration of multiples: Applications and challenges: The Leading Edge, v. 34, p. 780-786.

Yilmaz, Ö., 2001, Seismic data analysis: Processing, inversion, and interpretation of seismic data: Tulsa, OK, Society of Exploration Geophysicists

Zhu, X., P. Valasek, B. Roy, S. Shaw, J. Howell, S. Whitney, N. D. Whitmore, and P. Anno, 2008, Recent applications of turning-ray tomography: Geophysics v. 73, p. VE243-VE254.